# High-dimensional single-cell definition of CLL T cells identifies Galectin-9 as novel immunotherapy target

Llaó Cid L[1,*], Wong JKL[1,*], Fernandez Botana I[2,3], Paul Y[1], Wierz M[2], Flörchinger A[1,4], Gonder S[2,3], Pagano G[2,3], Chazotte M[5], Bestak K[5], Schifflers C[1], Iskar M[1], Roider T[6], Czernilofsky F[6], Bruch P-M[6,7], Mallm JP[8], Cosma A[9], Campton DE[10], Gerhard-Hartmann E[11], Rosenwald A[11], Colomer D[12], Campo E[12], Schapiro D[5,13], Dietrich S[6,7], Lichter P[1,14], Moussay E[2,#], Paggetti J[2,#], Zapatka M[1,#], Seiffert M[1,#,§]

[1] Division of Molecular Genetics, German Cancer Research Center, Heidelberg, Germany;

[2] Tumor Stroma Interactions, Department of Cancer Research, Luxembourg Institute of Health, Luxembourg, Luxembourg;

[3] Faculty of Science, Technology and Medicine, University of Luxembourg, Esch-sur-Alzette, Luxembourg;

[4] Faculty of Biosciences, University of Heidelberg, Heidelberg, Germany;

[5] Institute for Computational Biomedicine, Heidelberg University Hospital, Heidelberg, Germany;

[6] Department of Medicine V, Hematology, Oncology and Rheumatology, University of Heidelberg, Heidelberg, Germany;

[7] Department of Hematology, Onology and Clinical Immunology, University Hospital Düsseldorf, Düsseldorf, Germany

[8] scOpenLab, German Cancer Research Center, Heidelberg, Germany;

[9] National Cytometry Platform, Luxembourg Institute of Health, Luxembourg, Luxembourg;

[10] RareCyte, Seattle, WA, USA;

[11] Institute for Pathology, University of Würzburg, Würzburg, Germany;

[12] Institut d'Investigacions Biomèdiques August Pi i Sunyer (IDIBAPS), Hematopathology Unit, Hospital Clinic, CIBERONC, Barcelona, Spain;

[13] Institute of Pathology, Faculty of Medicine, Heidelberg University Hospital and Heidelberg University, Heidelberg, Germany;

[14] National Center for Tumor Diseases (NCT) Heidelberg, a partnership between DKFZ and Heidelberg University, Heidelberg, Germany

* equal contribution

[#] equal contribution

[§] corresponding author

**Contact information for correspondence:**

Martina Seiffert

Molecular Genetics (B060), German Cancer Research Center (DKFZ)

Im Neuenheimer Feld 280, 69120 Heidelberg, Germany

Tel.: +49-6221-42 4586, Fax: +49-6221-42 4639

Email: m.seiffert@dkfz.de

**Keywords:**

CLL; single-cell RNA-seq; mass cytometry; spatial analysis; multiplex imaging; T cell exhaustion; tumor microenvironment; Galectin-9; TIM3

**Abstract**

Failure of cancer immunotherapy is linked to T cell exhaustion. To decipher the underlying mechanisms, we explored the T cell landscape in blood, bone marrow and lymph node samples of patients with chronic lymphocytic leukemia (CLL), and spleen samples of a CLL mouse model. By single-cell RNA-sequencing, mass cytometry (CyTOF), and multiplex image analysis of tissue microarrays, we identified a disease-specific accumulation of distinct regulatory T cell subsets and T cell exhaustion stages and their trajectories in CLL lymph nodes. Integration of T cell receptor sequencing data revealed a clonal expansion of $CD8^+$ precursor exhausted T cells ($T_{PEX}$), suggesting their CLL reactivity. Interactome analyses identified the TIM3 ligand Galectin-9 as a novel immunoregulatory molecule in CLL. Blocking of Galectin-9 in CLL-bearing mice slowed down disease development and reduced the number of TIM3-expressing T cells. Galectin-9 expression correlated with shorter survival of patients with CLL, renal cell carcinoma or glioma.

**Statement of significance**

Our findings for the first time define the T cell landscape in CLL lymph nodes and reshape the current understanding of T cell exhaustion in this malignancy. They further introduce Galectin-9 as novel immune checkpoint with a high potential to overcome resistance to PD1 targeting drugs in CLL and beyond.

## Introduction

Failure of response to immune checkpoint inhibitors (ICI) is commonly seen in cancer patients with unknown causes and predictors, limiting the use of these novel immunotherapy approaches. B cell lymphomas develop in lymph nodes (LNs), the site of T cell priming and activation in infections and cancer. Even though there is a constant interaction of malignant B cells with $CD4^+$ and $CD8^+$ T cells in this tissue, adaptive immune control fails and response to ICI is very limited in patients with B cell lymphomas. In particular, very low response rates to anti-PD1 antibodies were observed in patients with chronic lymphocytic leukemia (CLL) (Ding et al., 2017; Xu-Monette et al., 2018), which is a neoplasm of mature B cells that accumulate in LNs and blood. In contrast to patients with acute lymphocytic leukemia (ALL), also response rates to CD19 CAR-T cell therapy remain below the expectations in CLL (Cappell et al., 2020). A lack of fit and functional T cells is discussed as a main limitation explaining the failure of immunotherapy responses in CLL and beyond (Fraietta et al., 2018; van Bruggen et al., 2019). Chronic exposure of T cells to tumor (neo)antigens and an immune suppressive microenvironment lead to their exhaustion and dysfunction (Blank et al., 2019). Whereas terminally exhausted T cells, characterized by high PD1 expression levels and expression of TOX, fail to reactivation by ICI, their precursor state that expresses lower levels of PD1 and is positive for TCF-7, harbors self-renewal capacity and the ability to control tumor development upon ICI treatment (Im et al., 2016; Scott et al., 2019; Utzschneider et al., 2016). The presence of these cell states has been confirmed in CLL patients and mouse models (Hanna et al., 2021), even though a characterization of T cells in CLL LNs is lacking due to the limited access to respective samples. Current efforts aim at characterizing mechanisms of T cell exhaustion in cancer and at identifying novel therapeutic targets to overcome this limitation.

Here, we applied single-cell RNA sequencing (scRNA-seq) and mass cytometry (CyTOF) of LNs, peripheral blood (PB) and bone marrow (BM) samples from patients with CLL, as well as tumor-free reactive lymph nodes (rLN) from healthy controls, combined with multiplex imaging of LN tissue sections and microarrays to characterize the distribution, phenotype, and function of T cells under chronic exposure to malignant cells. We show that CLL LNs constitute a unique niche, where clonally expanded $CD8^+$ T cells expressing CD39 and with exhausted phenotype are enriched in comparison to healthy LNs. We further defined cells with a signature of precursors of exhausted cells that accumulate in CLL LNs, as well as several types of regulatory T cells. The results of interactome analyses led us to target Galectin-9 in a CLL mouse model, which resulted in improved T cell function and an attenuated tumor development. Our analyses link Galectin-9 expression to survival of patients with CLL, kidney cancer or brain tumors.

## Results

### Definition of the T cell landscape in CLL using mass cytometry

To comprehensively characterize the T cell compartment associated with CLL, a large-scale and high-dimensional analysis of T cells from CLL patients as well as healthy controls (HC) was conducted using mass cytometry, scRNA-seq and multiplex imaging of tissue sections followed by integrative data analysis (Figure 1A). The patient cohort reflects the heterogeneity of CLL with respect to cell-of-origin, including both *IGHV* mutated (n=10) and unmutated (n=10) cases, as well as patients with the prevalent genetic aberrations (Suppl. Table 1). We performed mass cytometry profiling of T cells from 22 CLL LNs (including 2 patients with 2 time points), plus 7 paired PB and 3 paired BM samples, as well as 13 reactive LNs (rLNs) from HC using a panel of 42 antibodies (Key Resource Table) designed to identify and characterize naïve, memory, effector, regulatory and exhausted T cells. The analysis comprised 5.29 x$10^6$ T cells, with a median of 51,937 cells per sample (Suppl. Figure 1A-C). Unsupervised graph-based clustering based on the differential expression of the analyzed proteins grouped cells into 30 clusters which are presented as uniform manifold approximation and projection (UMAP) plot (Figure 1B, C, Suppl. Figure 2A). This approach led to the identification of 15 $CD4^+$ T cell clusters (including 4 $T_{REG}$ clusters), 9 $CD8^+$ T cell clusters, 4 double-negative T cell clusters, and 2 clusters with a mixture of $CD4^+$ and $CD8^+$ T cells (Figure 1D, Suppl. Figure 2B-C, and Suppl. Table 2). The expression of CD45RA, CD45RO, and CCR7 allowed for a general classification of T cells into naïve ($T_N$, $CD45RA^+$ $CD45RO^-$ $CCR7^+$), central memory ($T_{CM}$, $CD45RA^-$ $CD45RO^+$ $CCR7^+$), effector memory ($T_{EM}$, $CD45RA^-$ $CD45RO^+$ $CCR7^-$) and effector memory cells re-expressing CD45RA ($T_{EMRA}$, $CD45RA^+$ $CD45RO^-$ $CCR7^-$). The $CD8^+$ T cell subsets comprised 1 naïve (CD8 $T_N$), 1 central memory (CD8 $T_{CM}$), 3 subsets with a short-lived effector cell (SLEC) phenotype expressing TBET and KLRG1 (CD8 $T_{EMRA}$ TBET, CD8 $T_{EMRA}$ TBET, and CD8 $T_{EMRA}$ NCAM) (Joshi et al., 2007; Obar et al., 2011), and 4 effector memory subsets with a higher expression of the cytotoxic molecule granzyme K (GZMK) and an increasing expression of exhaustion-related molecules such as the inhibitory receptors PD1 and TIGIT, the TFs EOMES and TOX, and the ectoenzymes CD38 and CD39 (CD8 $T_{EM}$ GZMK, CD8 $T_{EM}$ TBET GZMK, CD8 $T_{EX}$ CD38, and CD8 $T_{EX}$ CD39) (McLane et al., 2019). The $CD4^+$ T cell subsets comprised 1 naïve (CD4 $T_N$), 3 central memory (CD4 $T_{CM1}$ CCR7, CD4 $T_{CM2}$ CD25, and CD4 $T_{CM3}$), 1 follicular helper ($T_{FH}$), and 6 effector memory subsets. Of these, two expressed TBET and KLRG1, resembling SLEC subsets (CD4 $T_{EM}$ NCAM, and CD4 $T_{EM}$ TBET), while 3 of them expressed higher levels of PD1 and TIGIT (CD4 $T_{EM}$ PD1), CTLA4 and CD38 (CD4 $T_{EM}$ CTLA4), or CD39 (CD4 $T_{EM}$ CD39). The last CD4 $T_{EM}$ subset expressed EOMES, GZMK and PD1 (CD4 $T_{EM}$ GZMK), and shares therefore characteristics of T regulatory type 1 cells ($T_R1$) and $CD4^+$ T cells with cytotoxic properties (Oh and Fong, 2021; Roessner et al., 2021). In addition,

FOXP3 expression identified 4 $T_{REG}$ clusters within the $CD4^+$ T cells, 2 with a central memory phenotype (CD4 $T_{REG\text{-}CM1}$ and CD4 $T_{REG\text{-}CM2}$), and 2 subsets with an activated inhibitory phenotype (CD4 $T_{REG}$ PD1 and CD4 $T_{REG}$ CD39). CD4 and CD8 double negative (DN) $CD3^+$ T cells comprised 2 clusters with a phenotype similar to CD8 SLEC subsets (DN $T_{EM}$ KLRG1 and DN $T_{EMRA}$ TBET), and 2 cytotoxic clusters expressing GZMK and EOMES as well as CD38 (DN $T_{EMRA}$ CD38) or the transcription factor HELIOS (DN $T_{EM}$ HELIOS). A $KI67^+$ proliferative subset ($T_{PR}$), as well as a cluster with high expression of ICOS ($T_{EM}$ ICOS) were both composed of $CD4^+$ and $CD8^+$ T cells.

To identify relationships between the T cell populations present in the CLL LNs, we correlated the subset frequencies of all individual CLL LN samples (n = 20, excluding the second time point of 2 samples, Figure 1E). Naïve $CD4^+$ and $CD8^+$ T cells as well as $CD4^+$ and $CD8^+$ T cells with a SLEC phenotype were significantly associated with each other, indicating that the LN tumor microenvironment (TME) is similarly influencing the differentiation of these cell states both in $CD4^+$ and $CD8^+$ T cells.

Spatial analyses of immune cell populations by multiplex immunofluorescence staining of a tissue microarray (TMA) of 42 CLL LN samples confirmed the presence and colocalization of malignant B cells with T cells in the tissue (Figure 2A, Suppl. Figure 3A-B). Quantification of the frequencies of the major immune cell subsets in the tissues revealed a positive correlation for $CD8^+$ $PD1^-$ and CD8 $PD1^+$ T cells, for myeloid cells and CD4 $T_{REG}$, and the strongest correlation for CD4 $T_{REG}$ and $PD1^+$ $CD8^+$ T cells (Figure 2B, Suppl. Figure 3C) which is in line with a role of CD4 $T_{REG}$ in promoting the accumulation of dysfunctional $CD8^+$ T cells (Sawant et al., 2019). We next quantitatively assessed the spatial cell-cell interactions by calculating the enrichment of pairwise interacting cell types for all cores using Giotto (Dries et al., 2021). This confirmed that the physical interaction between CD8 $PD1^+$ T cells and CD4 $T_{REG}$ as well as CD4 $PD1^+$ T cells and CD4 $T_{REG}$ is significantly enriched (Figure 2C-D, Suppl. Figure 3D).

**CLL LNs represent a distinct niche enriched with immunosuppressive T cell phenotypes**

We next examined the distribution of T cell immunophenotypes across the three different tissues analyzed in CLL. The sample composition of PB and BM was similar, but differed from LN samples (Figure 3A-B, Suppl. Figure 4A), suggesting that tissue cues significantly determine T cell composition. PB and BM samples were enriched in SLEC T cells, such as CD8 $T_{EM}$ TBET, CD4 $T_{EM}$ TBET, and DN $T_{EMRA}$ TBET, while CLL LNs contained higher frequencies of exhausted T cells (CD8 $T_{EX}$ CD39 and CD8 $T_{EX}$ CD38), CD4 $T_{EM}$ GZMK cells, CD4 $T_{FH}$ cells, several CD4 $T_{REG}$ subsets (CD4 $T_{REG\text{-}CM1}$, CD4 $T_{REG}$ PD1, and CD4 $T_{REG}$ CD39), as well as proliferating cells ($T_{PR}$) (Figure 3C). Even though the abundancies among

cell clusters within the tissue types correlated, no significant associations of the frequencies of cell subsets between PB and LN samples of the same patient were identified, underscoring a differential composition of T cell subsets between tissues (Suppl. Figure 4B).

The comparison of cell subset frequencies between CLL LNs and rLNs revealed that higher percentages of cytotoxic CD8 $T_{EM}$ GZMK as well as exhausted $CD8^+$ T cells (CD8 $T_{EX}$ CD39 and CD8 $T_{EX}$ CD38) were present in CLL LNs (Figure 3D). Within the CD4 compartment, CD4 $T_{EM}$ GZMK cells and all CD4 $T_{REG}$ clusters (CD4 $T_{REG\text{-}CM1}$, CD4 $T_{REG\text{-}CM2}$, CD4 $T_{REG}$ PD1, and CD4 $T_{REG}$ CD39) were also enriched in CLL LNs, in addition to proliferating $T_{PR}$ cells and DN $T_{EM}$ HELIOS cells (Figure 3D). Collectively, these results suggest that CLL LNs constitute a distinct niche where malignant B cell accumulation induces an immunosuppressive microenvironment with an enrichment of regulatory T cells and exhausted cytotoxic T cells.

Next, we examined the relation of clinical features to a distinct T cell composition in the CLL LNs. We detected a strong negative association between age of the patients and the frequency of naïve $CD8^+$ T cells (Suppl. Figure 4C, Suppl. Table 3) which is in line with published data (Gupta et al., 2004). In addition, the frequencies of 2 CD4 $T_{REG}$ clusters (CD4 $T_{REG\ CM2}$ and CD4 $T_{REG}$ PD1) showed a positive correlation with age (Suppl. Figure 4D, E). We did not observe significant associations between the frequencies of T cell clusters with sex or the clinical stage of the patients (Suppl. Table 3).

**Definition of T cell exhaustion states in CLL LNs by single-cell RNA-sequencing**

Next, single-cell RNA-seq of T cells from CLL LNs was performed to characterize their transcriptional profile and clonal diversity. $CD3^+$ T cells and a small spike-in population of CLL cells from LN samples of 5 CLL patients were FACS-sorted and subjected to scRNA-seq using the 10X Genomics platform, yielding 8,825 cells with an average of 4,577 reads per cell and a median of 1,475 genes per cell (STAR methods, Suppl. Figure 5A). Using unsupervised graph-based clustering, we identified 13 clusters presented in a UMAP plot (Figure 4A, STAR methods), for which we assigned an identity based on the differential gene expression of each cluster compared to the rest of the cells (Figure 4B). All cell clusters were shared among patients although at different proportions (Figure 4C, Suppl. Figure 5B). Clusters were defined as CLL cells, a small cluster of dendritic cells (DCs), 6 $CD4^+$ T cell subsets, 4 $CD8^+$ T cell subsets, and a $KI67^+$ proliferating T cell cluster ($T_{PR}$) which contained both $CD4^+$ and $CD8^+$ T cells (Figure 4A, B). More specifically, both $CD4^+$ and $CD8^+$ naïve (CD4 $T_N$ and CD8 $T_N$) T cells were defined based on the expression of marker genes such as *SELL*, *CCR7* and *IL7R*; regulatory $CD4^+$ T cells (CD4 $T_{REG}$) were identified by high expression of *FOXP3*, *IL2RA* and *IKZF2*; a heterogeneous cluster of cells containing mainly follicular helper $CD4^+$ T cells (CD4 $T_{FH}$) was defined by the expression of *CXCR5*, *CD200*,

*TOX2* and *TOX* (Suppl. Figure 5C, D), the small proportion of $CD8^+$ T cells in this cluster is in line with a shared transcriptional program of exhausted $CD8^+$ T cells with $T_{FH}$ (Im et al., 2016). Conventional $CD4^+$ T cells with a central memory phenotype were identified by the high expression of *IL7R, CD40LG, KLRB1* as well as *CD69* (CD4 $T_H$ CD69) or *ITGB1* and *KLF2* (CD4 $T_H$ KLF2) in accordance with published data of other B cell lymphoma (Roider et al., 2022). A heterogeneous cluster mainly comprising $CD4^+$ T cells expressed memory marker and effector molecule genes such as *GZMK*, resembling the CD4 $T_{EM}$ GZMK subset that shares features with $T_R$1-like cells, identified by mass cytometry (Figure 1B). $CD8^+$ effector memory subsets were characterized by a higher expression of effector molecule genes like *CCL5, NKG7, PRF1*, *GZMA* and *GZMK*. One subset expressed generally lower levels of these genes and high levels of *LYAR* (CD8 $T_{EM}$), another expressed higher levels of *CCL5* (CD8 $T_{PEX}$), and resembled the CD8 $T_{EM}$ GZMK cluster identified by mass cytometry (Figure 1B), and a third showed elevated expression of genes related to exhaustion such as *HAVCR2* (coding for TIM3), *LAG3, ENTPD1* (CD39), *PDCD1* (PD1), *CTLA4* and *TIGIT* (CD8 $T_{EX}$), and therefore resembled the two $T_{EX}$ clusters defined in the CyTOF data by high expression of these exhaustion markers (Figure 1B). Notably, the later subset expressed highest levels of the exhaustion signature from Zheng *et al*. (Zheng et al., 2021) (Figure 4D) confirming its dysfunctional state, while CD8 $T_{PEX}$ cells presented the highest score of the precursor exhausted signatures from Guo *et al*. (Guo et al., 2018) (Figure 4E) and Andreatta M *et al*. (Andreatta et al., 2021) (Suppl. Figure 5E) suggesting that these cells constitute a precursor state of exhausted $CD8^+$ T cells commonly named $T_{PEX}$ cells (Kallies et al., 2020). Subset clustering and definition were in agreement with the annotation from the pbmc3k signatures from Hao *et al*. (Hao et al., 2021) supporting the validity of our annotations (Suppl. Figure 5F). In addition, the frequency of the main T cell clusters was comparable and positively correlated between scRNA-seq and mass cytometry in the 4 samples analyzed by both techniques (Suppl. Figure 5G, H), underscoring the robustness of our data.

To delineate the relationship between T cell states, we performed trajectory analyses of $CD4^+$ and $CD8^+$ T cells by destiny (Angerer et al., 2016). When defining CD8 $T_N$ cells as the starting point of the differentiation path, we observed a bifurcation into two branches, one containing CD8 $T_{EM}$ cells and the other CD8 $T_{PEX}$ cells, from which $T_{EX}$ cells diverged and constituted a terminal state (Figure 4F, Suppl. Figure 5I). When inspecting the differentiation path from CD8 $T_N$ to CD8 $T_{EM}$, four clusters of differentially expressed genes (DEGs) were identified along the trajectory. Naïve marker genes (*LEF1, SELL*) were highly expressed in the first cluster, the second included the transcription factor *KLF2* and *IL6R*, the third activation marker genes (*CD69* and *DUSP1*), and the fourth effector molecule genes (*GZMH, NKG7, GZMA and FAS*) (Figure 4G). The differentiation path from CD8 $T_N$ to CD8 $T_{PEX}$ and CD8 $T_{EX}$ was also comprised of four clusters of DEGs, with naïve marker genes (*SELL*, *IL7R*

and *CCR7*) expressed at the beginning, followed by genes associated with activation (such as *CD69*) and cytotoxic function (*GZMK*), and genes related to exhaustion (*LAG3, EOMES, TIGIT, CD38* and *HAVCR2*) that were highest at the end of the trajectory (Figure 4H). This data suggests GZMK$^+$ CD8$^+$ T cells as a precursor state of terminally exhausted CD8$^+$ T cells which is in line with previously published data (Liu et al., 2022). Together with our CyTOF results that showed an accumulation of the CD8 $T_{EM}$ GZMK precursor state and terminally exhausted CD8$^+$ T cells in CLL LNs (Figure 3D), these findings suggest cancer-driven exhaustion of CD8$^+$ T cells in the lymphatic tissue of patients with CLL.

The CD4$^+$ T cell trajectory followed a similar pattern as CD8$^+$ T cells, starting with naïve genes (*SELL, TCF7* and *IL7R*), followed by genes for activation and effector molecules (*CD44, CXCR3,* and *GZMM*), and then by exhaustion-related genes (*LAG3, EOMES, LAYN, BTLA,* and *IRF4*) (Figure 4I, J; Suppl. Figure 5J), indicating a cancer-driven exhaustion also of CD4$^+$ T cells. The CD4 $T_{FH}$ and CD4 $T_{REG}$ cell clusters were diverting into two branches of the trajectory already at an early stage (Figure 4I).

**Effector memory CD8 T cells resembling precursors of exhausted cells are clonally expanded in CLL LNs**

The reconstruction of the T cell receptor (TCR) sequences at the single-cell level allowed us to examine the clonal diversity of T cells within the identified subsets. T cells that shared the same TCR sequence with at least one other cell were defined as clonal, and clone sizes of small (2-5 cells), medium (6-20 cells), large (21-100 cells) and hyperexpanded (101-500 cells) were identified. This data showed a major clonal expansion of CD8$^+$ T cells (ranging from 18% to 69%), but not CD4$^+$ T cells (4% to 26%) in the 5 CLL LN samples, and no correlation between the expansion rate of CD4$^+$ and CD8$^+$ T cells (Figure 5A). A comparison of the TCR sequences of the major clones with VDJdb verified that none of these TCRs were linked to known viral antigens (Suppl. Table 4). The clonal composition within the CD8$^+$ T cell compartment was highly variable among patients, with most samples showing mostly small and medium sized clones, and one sample (BC1) presenting one strongly dominating, hyperexpanded clone. Notably, CD8$^+$ T cell clonal expansion was enriched in the two CD8 $T_{EM}$ subsets and in CD8 $T_{EX}$ cells (Figure 5B, C) which explains the relative enrichment of the CD8 $T_{EM}$ cluster in the BC1 sample (Figure 4C) and suggests that these cells are tumor-reactive. Most TCR clones were confined to a specific T cell cluster, but some were shared between clusters with similar functional phenotypes, such as CD8 $T_{EM}$ and CD8 $T_{PEX}$ (Figure 5D, Suppl. Figure 6A). This suggests that either a dividing activated T cell produces cells with distinct transcriptional states, or that cells dynamically transit between two transcriptional states.

**CLL cells and T cells establish a unique interactome including Galectin-9 and TIM3 as ligand-receptor pair**

Next, we predicted receptor-ligand interactions between T cells and CLL cells in the LNs by performing differential interaction analysis using CellChat (Jin et al., 2021) on the basis of the public repository of ligand-receptor interactions from OmniPath (Türei et al., 2016). We included published scRNA-seq data from 5 rLNs (Aoki et al., 2020) in this analysis (Suppl. Figure 7A, B) to predict CLL-specific interactions. T cell subsets in both datasets were grouped into major functional types (CD4 $T_N$, CD8 $T_N$, CD4 $T_{FH}$, CD4 $T_{CM}$, CD4 $T_{REG}$, CD4 $T_{EM}$ and CD8 $T_{EM}$) to facilitate comparison. Predicted receptor-ligand interactions were prioritized by the probability of differential interaction across CLL LNs and rLNs. Overall, the number of inferred interactions was slightly higher in the CLL LNs compared to the rLNs (1828 vs. 1622; Suppl. Figure 7C). The highest number of predicted interactions was found for CLL cells and CD8 $T_{EM}$ cells, which act as senders and receivers of signals, both in an autocrine and paracrine manner (Figure 6A, B). These two cell types were predicted to strongly interact with each other and also with all other cell subsets. Inferred CLL-specific interactions included ligand-receptor pairs with known relevance in CLL, such as CD74-MIF (Reinart et al., 2013), and the chemokines CCL4 and CCL5 and their receptors (Burger et al., 2009; Kiaii et al., 2013) (Figure 6C). In addition, collagen and adhesion molecules and their binding partners (COL9A2/3 and ICAM-ITGAL) were predicted as novel interactions. Numerous inferred interactions between T cells and CLL cells were related to T cell inhibitory signals, such as HLA-LAG3 (Wierz et al., 2018), BTLA-CD247 (Karabon et al., 2020) and LGALS9-related circuits. Galectin-9 (encoded by *LGALS9*) is a known ligand of the inhibitory receptor TIM3 and its binding to TIM3 induces T cell death and thus contributes to tumor immune escape (Yang et al., 2008; Zhu et al., 2005). In CLL, Galectin-9 levels are increased in serum of patients (Pang et al., 2021b; Wdowiak et al., 2019; Xierenguli et al., 2020). Our scRNA-seq data identified CLL cells and dendritic cells as a source of Galectin-9, showing an increased *LGALS9* expression in CLL compared to rLNs (Figure 6D). The Galectin-9 binding partner TIM3 (encoded by *HAVCR2*) was detected in CD8 $T_{EX}$ cells in CLL LNs, but was absent in rLNs (Figure 6D). Multiplex immunofluorescence staining of CLL LN sections further confirmed the presence of TIM3 expressing $CD4^+$ and $CD8^+$ T cells in the tissue (Figure 6E).

**Galectin-9 blockade reduces CLL development in mice**

We next aimed to preclinically test the potential of Galectin-9 blockade in a mouse model of CLL. As the Eμ-TCL1 mouse line (Bichi et al., 2002) is the most explored and used *in vivo* model of CLL, we first performed single-cell RNA-seq to characterize the T cell compartment of mice that developed CLL-like disease after adoptive transfer of malignant B cells from this

mouse line (TCL1 AT). This allowed us to identify 13 clusters of T cells in the spleen of leukemic mice, including naïve, effector, effector memory, and regulatory T cell subsets (Suppl. Figure 8A, B, C). When integrating TCR-seq data, it became clear that one of the two analyzed samples (#107) harbored a hyperexpanded $CD4^+$ T cell clone showing an effector phenotype and *Gzmk* expression, which was not the case for the second sample (#110) that contained a large $CD8^+$ effector memory T cell cluster (Suppl. Figure 8D, E). The clonally expanded $CD4^+$ effector T cells in sample #107 contained a cluster of cells expressing exhaustion-related genes. This data suggests the occurrence of $CD4^+$ T cell-driven adaptive immune control in TCL1 AT mice which is in line with observations in other tumor mouse models and patients with cancer (Oh and Fong, 2021; Oh et al., 2020; Quezada et al., 2010; Xie et al., 2010).

Flow cytometry analyses showed that the vast proportion of malignant B cells in the spleen and bone marrow of TCL1 AT mice expressed Galectin-9, which was not the case for B cells from wild-type (WT) mice (Figure 7A, Suppl. Figure 8F). Also, higher frequencies of Galectin-9-positive CLL cells were detected in lymph nodes and PB of TCL1 AT mice compared to WT mice (Suppl. Figure 8F). We further observed TIM3-positive T cells in tumor-bearing TCL1 AT but not WT mice, with the highest frequencies detected in CD8 $T_{EF}$ and CD4 $T_{REG}$ cells (Figure 7B).

To test the potential of Galectin-9 as novel therapy target for CLL, we treated CLL-bearing TCL1 AT mice with Galectin-9-blocking antibodies for 20 days (Figure 7C). By a weekly assessment of CLL cell counts in the blood of the mice, a deceleration of leukemia development was observed by anti-Galectin-9 compared to isotype control treatment (Figure 7D). At the endpoint of the experiment, 7 weeks after TCL1 AT, a reduced spleen weight and lower numbers of CLL cells were detected in the spleen and lymph nodes of the mice receiving anti-Galectin-9 (Figure 7E, F). We further analyzed T cells in the spleen and lymph nodes at the endpoint and did not observe major differences in the numbers of $CD8^+$ T cells, conventional $CD4^+$ T cells, or $CD4^+$ $T_{REG}$, nor in their activation state measured as % of $CD44^+$ cells (Suppl. Figure 9A, B, C). We detected however, a lower frequency of $CD39^+$ and a higher frequency of $CD107A^+$ $CD8^+$ T cells in the treated mice (Figure 7G, H), suggesting a higher functionality of $CD8^+$ T cells upon anti-Galectin-9 treatment. The most drastic differences were observed in the frequencies of $TIM3^+$ T cells, which were severely decreased for $CD8^+$ T cells, conventional $CD4^+$ T cells and $CD4^+$ $PD1^+$ $T_{REG}$ cells in the spleen and to a lower degree also in LNs (Figure 7I-K, Suppl. Figure 9D) which is in line with the proposed role of Galectin-9 in preventing apoptosis of $TIM3^+$ T cells (Zhu et al., 2005). Based on these data, we suggest that anti-Galectin-9 treatment results in a better immune control of CLL via suspending the immune suppressive activity of TIM3 on CLL-associated T cells.

**High Galectin-9 expression is associated with shorter survival of patients with CLL, kidney cancer and brain tumors**

Next, we explored the expression of *LGALS9* across cancer entities using publically available TCGA data (Li et al., 2021). A comparison of tumor and respective normal tissue revealed a higher expression in about half of the cancer types analyzed (Figure 8A, Suppl. Figure 10A). To estimate the relevance of Galectin-9 in CLL development, we analyzed a previously published proteome data set of CLL cells (Herbst et al., 2022). Dividing patients into two groups based on the median level of Galectin-9 expression clearly demonstrated a significantly shorter treatment-free survival in cases with high Galectin-9 expression (Figure 8B). Dividing this cohort of patients into the two main prognostic groups, namely cases with unmutated or mutated *IGHV* gene locus, we observed higher Galectin-9 protein expression in the *IGHV*-unmutated group which has a worse overall prognosis (Suppl. Figure 10B). Within this group, higher Galectin-9 protein levels clearly predicted shorter treatment-free survival (Suppl. Figure 10C) which was not the case in the *IGHV*-mutated group of CLL patients (Suppl. Figure 10D).

We further analyzed the prognostic value of *LGALS9* expression across cancer types and identified significant associations of high levels of *LGALS9* with shorter overall survival for renal cell carcinoma and glioma patients (Figure 8C+D). By exploring published scRNA-seq data of these two cancer types, we observed *LGALS9* expression mainly in tumor-associated myeloid cells (Figure 8E-J). Of interest, myeloid cell infiltration has been linked to immune suppression and worse outcome of patients for renal cell carcinoma and glioma (Jikuya et al., 2020; Şenbabaoğlu et al., 2016; Vuong et al., 2019; Zhang et al., 2021). Altogether this suggests Galectin-9 as novel potential target for immunotherapy in CLL and likely other cancer entities.

## Discussion

T cell exhaustion is considered as one of the main reasons for failure of immunotherapies. However, its contribution to resistance of patients with B cell malignancies to such treatments has not been explored so far. Our study provides, for the first time, a single-cell-resolved analysis of the T cell landscape in blood and tissue samples of CLL, the most common leukemia in the Western world. CLL is a disease that is dependent on microenvironmental stimuli provided by the lymph node niche that drive growth and survival of malignant cells which are quiescent in peripheral blood. Most previous studies characterized disease-associated alterations in the T cell compartment in blood samples. Our data now clearly show that exhaustion of cytotoxic T cells and accumulation of regulatory T cells is very prominent in the lymph nodes but not in blood, suggesting the lymphoid tissue as the site of cancer-directed immune responses in CLL.

Our multimodal omics approach allowed us to integrate scRNA-seq, CyTOF, and multiplex imaging of lymph nodes to obtain an unprecedented resolution of the T cell landscape in CLL. The three complementary data sets enabled the identification and characterization of different stages of T cell exhaustion and their clonal expansion in CLL lymph nodes, as well as several regulatory T cell clusters that are in terms of abundance and spatial localization linked to $PD1^+$ $CD8^+$ effector T cells. In addition to terminally exhausted CD8 T cells, called $T_{EX}$, the lymph nodes contain a population of cells that resembled the previously described precursor cells of exhaustion, (Im et al., 2016; Utzschneider et al., 2016), now frequently named $T_{PEX}$ (Kallies et al., 2020), that share features with memory T cells and have a high *GZMK* expression (Liu et al., 2022). These cells have self-renewal capacity which likely explains our observation of a strong accumulation of TCR clonotypes in this population. Our data identifying such cells in CLL LNs is in line with recent studies demonstrating their presence in tumor-draining LNs of solid cancer where they are essential for efficient response to ICI therapy (Connolly et al., 2021; Huang et al., 2022).

CLL cells in lymph nodes are densely packed together with T cells and interactome analyses using the scRNA-seq data suggested a list of known and novel molecular interactions between the two cell types. It is well-accepted that CLL cells depend on microenvironment-derived signals for survival and proliferation, and the identified interactions including MIF-CD74 (Reinart et al., 2013), CCL4 and CCL5 (Kiaii et al., 2013), and INFG (Buschle et al., 1993) are part of this support. Further, the interactome study inferred several inhibitory molecular interactions including BTLA-CD247, CTLA4 and Galectin-9 (encoded by *LGALS9*). Galectin-9 is a known ligand of TIM3, an inhibitory receptor that is expressed on exhausted T cells (Wolf et al., 2020). Even though we detected very low levels of *HAVCR2* (encoding TIM3) by scRNA-seq, we confirmed the presence of TIM3-positive T cells in CLL

lymph node tissue, and assumed an involvement of this interaction in immune escape as Galectin-9 binding to TIM3 promotes $CD4^+$ $T_{REG}$ development in CLL (Pang et al., 2021a).

TIM3-targeting antibodies now enter clinical trials and show the first promising anti-tumor activity in patients with advanced solid tumors (Curigliano et al., 2021). These antibodies block the interaction of TIM3 with phosphatidylserine and CEACAM1, but only partially the binding to Galectin-9 (Sabatos-Peyton et al., 2020; Sabatos-Peyton et al., 2018). Blocking antibodies targeting Galectin-9 can overcome this limitation and suppress tumor growth in combination with chemotherapy in a breast cancer mouse model (de Mingo Pulido et al., 2018). This activity was dependent on $CD8^+$ T cells, which is in line with our observation of an enhanced $CD8^+$ effector function in anti-Galectin-9 treated TCL1 mice.

Binding of Galectin-9 to TIM3 on T cells induces cell death, thereby limiting adaptive immunity (Zhu et al., 2005). This raises the question of why terminally exhausted T cells harboring TIM3 expression persist in the tumor microenvironment. Recent data showed that PD1, via physically interacting with Galectin-9 and TIM3, protects T cells from apoptosis (Yang et al., 2021). As a consequence, $PD1^+$ $TIM3^+$ T cells accumulate in tumors even in the presence of enhanced levels of Galectin-9. Blockade of Galectin-9 *in vitro* and in mouse models results in enhanced T cell survival and improved anti-tumor immunity, especially in combination with co-stimulatory anti-GITR treatment (Yang et al., 2021). In accordance, anti-Galectin-9 treatment of TCL1 mice diminished $PD1^+$ $TIM3^+$ T cells along with a reduction in tumor development.

Besides improving T cell responses, antibody-mediated targeting of Galectin-9 on B-ALL cells induces DNA damage, alters cell cycle progression, and promotes apoptosis *in vitro* and significantly extends the survival of mice with aggressive B-ALL (Lee et al., 2022). Accordingly, we cannot exclude that a similar direct activity on CLL cells contributes to the delayed leukemia development in TCL1 mice. Further, ligand activation of Galectin-9 in the tumor microenvironment of pancreatic ductal adenocarcinoma results in tolerogenic macrophage programming and adaptive immune suppression (Daley et al., 2017). As CLL is dominated by immunosuppressive myeloid cells (Hanna et al., 2019), Galectin-9 blockade potentially ameliorates this milieu which likely contributes to a better T cell function.

In line with these mechanistic findings, *LGALS9* expression is higher in tumor compared to respective normal tissue across many cancer types. In CLL, we defined the malignant B cells as the main source of Galectin-9, even though myeloid cell types likely contribute to its expression. In solid cancers however, Galection-9 is likely produced mainly by myeloid cells, like tumor-associated macrophages or myeloid-derived suppressor cells. This also explains that both the abundance of tumor-infiltrating myeloid cells and high expression of *LGALS9* predict shorter survival of patients with renal cell carcinoma or glioma (Jikuya et al., 2020; Şenbabaoğlu et al., 2016; Vuong et al., 2019; Yeo et al., 2022; Zhang et al., 2021).

Prediction of outcome is restricted in CLL to cases with unmutated *IGHV* gene locus, which show significantly higher Galectin-9 expression compared to cases with mutated *IGHV* and are generally considered as the worse prognostic group of patients (Damle et al., 1999; Hamblin et al., 1999). As the Eμ-TCL1 mouse model mimics CLL with unmutated immunoglobulins (Yan et al., 2006), our data suggests treatment efficacy of anti-Galectin-9 specifically for this more aggressive form of CLL.

Our study focused on an in-depth characterization of the T cell landscape in CLL and we excluded myeloid cells from the analysis, which represents a limitation of our analysis. Immunosuppressive interactions of CLL-associated myeloid cells and T cells contribute to immune escape in CLL (Hanna et al., 2016; Jitschin et al., 2014), but their analysis requires fresh tissue samples to prevent a biased loss of myeloid cell subsets by freezing and thawing, and such samples are rarely available. As suppression of anti-tumor immunity is complex and multifactorial, obtaining a complete picture of all cell types and their interactions with the cancer cells will be necessary for the development of combinatorial treatment targeting multiple immune cell types and checkpoints to avoid immune escape and resistance to therapy. The data provided here suggest that Galectin-9 is an attractive novel therapy target for immunotherapy in CLL and likely beyond in other cancers.

## Figure Legends

**Figure 1: Profiling of the T cell landscape in CLL tissues at the single-cell resolution**

**A)** Graphical overview of the study design. Mass cytometry analyses were performed on 13 rLNs, 7 CLL PB, 3 CLL BM and 22 CLL LNs, 15-color multiplex immunostaining was applied in an additional data set of 42 CLL LNs, and 5 CLL LNs were analyzed using scRNA-seq and TCR-seq. **B)** UMAP plot of 5.2 x$10^6$ $CD3^+$ T cells from 13 rLNs, 7 CLL PB, 3 CLL BM and 22 CLL LNs analyzed by mass cytometry identifying 30 clusters, including 15 for $CD4^+$ T cells, 9 for $CD8^+$ T cells, 2 clusters containing both $CD4^+$ and $CD8^+$ T cells, and 4 DN T cells. **C)** Projection of a selection of protein markers identifying T cell states. Cells are colored based on the normalized protein expression. **D)** Dot plot of the expression of marker genes in the 30 cell clusters. **E)** Heatmap showing the Pearson correlation coefficient and its associated p-value of cell subset proportions from the 20 CLL LNs, corresponding to the worst performing subset (for which the p-value was the highest) of all leave-one-out patient sample sets.

**Figure 2: PD-$1^+$ T cells reside in close proximity to $T_{REG}$ cells in CLL LNs**

**A)** Representative CLL LN-derived tissue core stained with 15-color Orion multiplex with cells colored according to subset identification. CLL cells are displayed as $B_{PR}$: Ki-$67^+$ proliferating B cells, and Other: mainly non-proliferating B cells. **B)** Pearson correlations of $PD1^+$ $CD8^+$ T cells and $T_{REG}$ frequencies determined by multiplex staining of 42 CLL LN cores. Each dot represents an individual patient. **C)** Representative CLL LN-derived tissue core (left image) and field of view (middle image) displaying FOXP3 (yellow), CD8A (red) and PD-1 (pink) staining. The right image displays cells identified as $T_{REG}$ and CD8 PD-$1^+$ T cells in yellow and purple dots, respectively. **D)** Boxplots (left) depicting the range of enrichment of pairwise interacting cell types for all cores (n = 42). Boxplots (right) showing the absolute number of interactions in log10 scale between pairwise interacting cell types across all cores. Colored by type of interaction, between same cell type (blue) or different cell types (red).

**Figure 3: The T cell composition of CLL LNs is distinct and enriched in regulatory and exhausted subsets**

**A)** Principal component analysis of all samples analyzed by mass cytometry based on cell subset frequencies. **B)** UMAP plots of T cells from rLNs, CLL PB, CLL BM and CLL LNs overlaid with a contour plot indicating the cell density. **C)** Boxplot showing cell subset abundances in LNs (n = 20), PB (n = 7) and BM (n = 3) of CLL patients. Statistical significance between CLL LNs and CLL PBs was assessed by limma on normalized cell counts. **D)** Boxplot showing cell subset abundances in CLL LNs (n = 20) and rLN (n = 13).

Each symbol represents an individual patient sample and statistical significance was tested by limma on normalized cell counts, *$p$<0.05, **<0.01, ***<0.001.

**Figure 4: Single-cell RNA-seq defines T cell states in CLL LNs**

**A)** UMAP plot of 8,576 cells from 5 CLL LNs analyzed by scRNA-seq identifying 13 clusters, including 6 for $CD4^+$ T cells, 4 $CD8^+$ T cells, proliferating $CD4^+$ and $CD8^+$ T cells, DCs and spiked in CLL cells. **B)** Dot plot of the expression of marker genes in the 13 cell clusters. **C)** Cell subset abundance in each sample (BC0, 1, 2, 3, and 9), with colors and numbers corresponding to the identified cell clusters. **D-E)** Violin plot of average expression levels of the exhaustion gene signature adapted from Zheng L, *et al* Science, 2021 (D), and the precursor exhaustion gene signature from Guo X, *et al* Nat Med, 2018 (E). **F)** Pseudotime trajectory across the 4 $CD8^+$ T cell subsets**. G)** Heatmap showing genes with significant expression changes along the trajectory from CD8 $T_N$ to CD8 $T_{EM}$ **H)** Heatmap showing genes with significant expression changes along the trajectory from $T_N$ to CD8 $T_{EX}$. Color represents z-scores. **I)** Pseudotime trajectory across the 6 $CD4^+$ T cell subsets**. J)** Heatmap showing genes with significant expression changes along the trajectory from CD4 $T_N$ to CD4 $T_{FH}$. Color represents z-scores.

**Figure 5: T cell clonal expansion in CLL is mainly restricted to CD8 $T_{EM}$ cells**

**A)** Bar plot indicating the percentage (rounded values are indicated) of single, small, medium, large and hyperexpanded sized clones in $CD8^+$ (left) and $CD4^+$ (right) T cells for each patient analyzed (n = 5). **B)** UMAP plot colored according to the T cell clone size based on the TCR-seq data. **C)** Graph showing the TCR Shannon diversity index for each T cell subset identified by scRNA-seq. The dot color corresponds to the UMAP cluster plot from Figure 4A. **D)** Chord diagram showing clone sharing from CD8 $T_{EM}$ and CD8 $T_{PEX}$. Only cells carrying expanded TCR sequence are presented in the circle. Cells sharing identical TCR sequences across clusters are summed and connected by bands.

**Figure 6: Interactome analyses of CLL LNs identify Galectin-9 as a potential therapeutic target**

**A)** Circle plot depicting the differential number of interactions between cell subsets in CLL LNs compared to rLNs. Thickness of bands represents the number of differential interactions between the two data sets, and increased interactions are depicted in red, decreased interactions in blue. **B)** Heatmap showing the differential number of interactions of CLL LNs versus rLNs. Rows and columns represent source and target subsets, respectively. Bar plots represent the total outgoing (right) and incoming (top) interactions scores respectively. **C)** Heatmap plot depicting a curated list of ligand-receptor pairs differentially upregulated in CLL

LNs compared to rLNs as identified via CellChat (Jin et al., 2021). The dot color and size represent the calculated communication probability and p-values of differential communication, respectively. The first 7 columns show interactions sent by CLL cells, while the last 7 columns show interactions received by CLL cells. **D)** Violin plots showing the expression distribution of *LGALS9* (top two plots) and *HAVCR2* (bottom plots) genes in the CLL LN data set and the rLN data set from Aoki *et* al. (Aoki et al., 2020). Each dot represents one cell. **E)** Representative microscopy images showing CD3, CD8, TIM3 and DAPI as single stains and overlayed image (left) in a CLL LN tissue section. Arrows indicate $CD3^+$ $CD8^+$ $TIM3^+$ cells.

**Figure 7: Blocking of Galectin-9 controls tumor growth in the TCL1 mouse model**

**A)** Representative contour plot and percentage of Galectin-$9^+$ B cells and CLL cells from spleen of WT and TCL1 AT mice, respectively (n = 5). **B)** Percentage of $TIM3^+$ cells out of CD8 $T_N$, CD8 $T_M$, CD8 $T_{EF}$, CD4 $T_{CONV}$ and $T_{REG}$ T cells in spleen of WT and TCL1 AT mice (n = 5). **C)** Schematic diagram of Galectin-9-blocking antibody treatment in TCL1 AT mice (n = 8-10). Analyses of T, myeloid and CLL cells were performed 7 weeks after treatment start. **D)** Absolute number of $CD19^+$ $CD5^+$ CLL cells in blood of isotype antibody- and anti-Galectin-9-treated mice. **E)** Spleen weight, and **F)** absolute number of $CD19^+$ $CD5^+$ CLL cells in spleen and lymph nodes of isotype antibody- and anti-Galectin-9-treated mice. **G)** Representative contour plot and percentage of $CD39^+$ cells out of $CD8^+$ T cells from spleen of isotype antibody- and anti-Galectin-9-treated mice. **H)** Representative contour plot and percentage of $CD107A^+$ out of $CD8^+$ T cells from spleen of isotype antibody- and anti-Galectin-9-treated mice. **I-K)** Representative contour plot and percentage of $PD1^+$ $TIM3^+$ cells out of $CD8^+$ T cells (I), $CD4^+$ $T_{CONV}$ (J), and $T_{REG}$ (K) cells from spleen of isotype antibody- and anti-Galectin-9-treated mice.

Each symbol represents an individual mouse, statistical significance was tested by unpaired t-test with Welch approximation, *$p$<0.05, **<0.01, ***<0.001. Bars indicate mean ± SEM.

**Figure 8: Elevated *LGALS9* expression correlates with poor survival in cancer patients**

**A)** *LGALS9* transcript levels in tumor (T) versus healthy (N) tissue in CESC (Cervical squamous cell carcinoma and endocervical adenocarcinoma), COAD (Colon adenocarcinoma), DLCL (Diffuse large B cell lymphoma), ESCA (Esophageal carcinoma), GBM (Glioblastoma multiforme), KIRC (Kidney renal clear cell carcinoma), KIRP (Kidney renal papillary cell carcinoma), LAML (Acute Myeloid Leukemia), LGG (Brain Lower Grade Glioma), LIHC (Liver hepatocellular carcinoma), OV (Ovarian serous cystadenocarcinoma), PAAD (Pancreatic adenocarcinoma), READ (Rectum adenocarcinoma), SKCM (Skin Cutaneous Melanoma), STAD (Stomach adenocarcinoma), TGCT (Testicular Germ Cell

Tumors), and UCEC (Uterine Corpus Endometrial Carcinoma) (Li et al., 2021). **B)** Time-to-treatment in CLL patients with high or low Galectin-9 protein levels (n = 63) (Herbst et al., 2022). **C-D)** Overall survival in renal cell carcinoma (C) and glioma (D) patients with high or low *LGALS9* transcript levels. **E-J)** Single-cell RNA-seq analysis of tumor samples in renal cell carcinoma (Bi et al., 2021) (E-G) and glioma (Abdelfattah et al., 2022) (H-J). E and H) UMAP plots identifying tumor, infiltrating immune cells and normal tissue cells from E) 8 renal cell carcinoma patients, and H) 9 glioma patients. F and I) UMAP plot displaying *LGALS9* expression. G and J) Violin plots of *LGALS9* expression.

## Supplementary Figure Legends

**Supplementary Figure 1 (related to Figure 1):**

**A)** Gating strategy used to select live, $CD45^+$ $CD3^+$ T cells: gates were placed on cells (Beads vs. Ir191), singlets (Ir193 vs. Ir191) and live cells ($Pt195^-$), which were gated and exported as .fcs files. $CD3^+$ cells were further analyzed. **B)** Number of T cells per analyzed sample. **C)** UMAP plot depicting sample distribution.

**Supplementary Figure 2 (related to Figure 1):**

**A)** Projection of all protein markers analyzed by mass cytometry. Cells are colored based on the normalized protein expression. **B)** Heatmap showing median protein expression of the 33 markers considered (columns) for each cluster (rows) identified. Both markers and clusters were grouped based on hierarchical clustering. **C)** Cell subset frequency for each cluster. Each dot represents one sample. Clusters are ordered from highest to lowest median frequency.

**Supplementary Figure 3 (related to Figure 2):**

**A)** Representative images of 15-color multiplex staining of tissue cores of CLL LNs. **B)** Frequency of all cell types identified using the 15-color multiplex staining. Colors represent the individual cell types, and each core is represented by the individual column – with cores from the same patient grouped together - in the bar plot (n = 42). “Other (mainly CLL)” cells make up the rest of the cells and are not depicted. **C)** Heatmap showing the Pearson correlation coefficient and its associated p-value of the multiplex staining cell subset proportions from the 42 CLL LN cores, corresponding to the worst performing subset of all leave-one-out patient samples. The correlation for each cell subset pair was then defined as the result among subsets for which the p-value was highest. Significant results are depicted with black borders. **D)** Heatmap showing the significance score of pairwise interacting cell types (columns) for each core (rows) (n = 42) as generated by Giotto. Cell type pairs and cores were both grouped based on hierarchical clustering.

**Supplementary Figure 4 (related to Figure 3):**

**A)** Hierarchical clustering (with Pearson correlation and complete linkage) of samples based on the T cell subset abundances in each sample. Cell subsets are color-coded as defined in Fig. 1B. Row annotations indicate sample condition (BM, bone marrow, LN, lymph node, and PB, peripheral blood), age (years) and tumor load (TL). **B)** Heatmap showing the Pearson correlation coefficient and its associated p-value of cell subset proportions from the 7-paired CLL LN and PB samples, corresponding to the worst performing subset of all leave-one-out

patient samples. The correlation for each cell subset pair was then defined as the result among subsets for which the p-value was highest. **C-E)** Pearson correlation plot between age and frequency of CD8 $T_N$ cells (C), $T_{REG\ CM2}$ cells (D), and $T_{REG}$ PD1 cells (E). Each symbol represents an individual patient sample.

**Supplementary Figure 5 (related to Figure 4):**

**A)** Gating strategy used to isolate live, $CD45^+$ $CD3^+$ T cells and CLL cells: gates were placed on cells (SSC-A vs FSC-A), singlets (FSC-H vs FSC-A) and live cells (Negative for viability dye). $CD45^+$ cells were further gated for CLL cells ($CD19^+$ $CD5^+$) or T cells ($CD19^-$ $CD3^+$). **B)** UMAP plot depicting sample distribution. **C)** UMAP plot of $T_{FH}$ cells. **D)** Heatmap of differentially expressed genes of the 4 clusters of $T_{FH}$ cells. **E)** UMAP plot colored by average expression of the precursor exhaustion gene signature from Andreatta *et al* (Andreatta et al., 2021), and **F)** according to PBMC3K data set (Hao et al., 2021) applied to the data set of 5 CLL LNs. **G)** Cell subset distribution of the major T cell subsets in the 4 CLL samples analyzed with scRNA-seq and mass cytometry. **H)** Pearson correlation of major T cell subset frequencies determined with scRNA-seq and the mass cytometry data for the 4 CLL patient samples analyzed with both techniques. **I-J)** $CD8^+$ (I) and $CD4^+$ (J) T cell subsets ordered by diffusion pseudotime.

**Supplementary Figure 6 (related to Figure 5):**

**A)** Chord diagram showing the expanded TCR clone sharing between the T cell subsets identified. Cells carrying identical TCR sequences are connected by bands.

**Supplementary Figure 7 (related to Figure 6):**

**A)** UMAP plot of 20,673 cells from 5 rLNs analyzed by scRNA-seq from Aoki *et* al. (Aoki et al., 2020) identifying 21 clusters, including 9 T cell clusters, 8 B cell clusters, proliferating cells, NK cells and DCs. **B)** UMAP plot where PBMC3K data set (Hao et al., 2021) was mapped to the 5 rLNs data set from Aoki *et* al. (Aoki et al., 2020). **C)** Number of inferred interactions between T cells and B cells in rLN samples, or T cells and CLL cells in CLL LN samples.

**Supplementary Figure 8 (related to Figure 7):**

**A)** UMAP plot of 6,201 cells from 2 TCL1 AT spleens analyzed by scRNA-seq identifying 13 clusters, including 11 T cells clusters, CLL cells and myeloid cells. **B)** UMAP plot depicting sample distribution. **C)** Dot plot of the expression of marker genes in the 13 cell clusters**. D)** UMAP plot colored according to the T cell clone size based on the TCR-seq data**. E)** Bar plot indicating the percentage (rounded values are indicated) of single, small, medium, large and

hyperexpanded sized clones in $CD8^+$ (left) and $CD4^+$ (right) T cells for the two mouse samples analyzed**. F)** Percentage of Galectin-$9^+$ B cells and CLL cells from bone marrow, lymph nodes and peripheral blood of WT and TCL1 AT mice. Each symbol represents an individual mouse, statistical significance was tested by unpaired t-test with Welch approximation, *$p$<0.05, **<0.01, ***<0.001.

**Supplementary Figure 9 (related to Figure 7):**

**A-B)** Absolute number of $CD4^+$ $T_{CONV}$, $T_{REG}$ and $CD8^+$ T cells in spleen (A) and lymph nodes (B) of isotype antibody- and anti-Galectin-9-treated mice. **C)** Percentage of $CD44^+$ cells out of $CD8^+$ and $CD4^+$ $T_{CONV}$ cells in spleen of isotype antibody- and anti-Galectin-9-treated mice. **D)** Percentage of $PD1^+$ $TIM3^+$ cells out of $CD8^+$, $CD4^+$ $T_{CONV}$ and $T_{REG}$ cells in lymph nodes of isotype antibody- and anti-Galectin-9-treated mice. Each symbol represents an individual mouse, and statistical significance was tested by unpaired t-test with Welch approximation, *$p$<0.05, **<0.01. Bars indicate mean ± SEM. Ns = not significant.

**Supplementary Figure 10 (related to Figure 8):**

**A)** *LGALS9* transcript levels in tumor versus healthy tissue in ACC (Adrenocortical Carcinoma), BLCA (Bladder Urothelial Carcinoma), BRCA (Breast invasive carcinoma) CESC (Cervical squamous cell carcinoma and endocervical adenocarcinoma), CHOL (Cholangiocarcinoma), COAD (Colon adenocarcinoma), DLBC (Lymphoid Neoplasm Diffuse Large B-cell Lymphoma), ESCA (Esophageal carcinoma), GBM (Glioblastoma multiforme), HNSC (Head and Neck squamous cell carcinoma), KICH (Kidney Chromophobe), KIRC (Kidney renal clear cell carcinoma), KIRP (Kidney renal papillary cell carcinoma), LAML (Acute Myeloid Leukemia), LGG (Brain Lower Grade Glioma), LIHC (Liver hepatocellular carcinoma), LUAD (Lung adenocarcinoma), LUSC (Lung squamous cell carcinoma), MESO (Mesothelioma), OV (Ovarian serous cystadenocarcinoma), PAAD (Pancreatic adenocarcinoma), PCPG (Pheochromocytoma and Paraganglioma), PRAD (Prostate adenocarcinoma), READ (Rectum adenocarcinoma), SARC (Sarcoma), SKCM (Skin Cutaneous Melanoma), STAD (Stomach adenocarcinoma), TGCT (Testicular Germ Cell Tumors), THCA (Thyroid carcinoma), THYM (Thymoma), UCEC (Uterine Corpus Endometrial Carcinoma), UCS (Uterine Carcinosarcoma) and UVM (Uveal Melanoma) (Li et al., 2021). **B)** Galectin-9 protein levels in *IGHV*-mutated versus *IGHV*-unmutated CLL patients. Each dot represents a patient. **C-D)** Time-to-treatment in C) *IGHV*-mutated and D) *IGHV*-unmutated CLL patients with high or low Galectin-9 protein levels (Herbst et al., 2022).

## Methods

*Patient samples*

Lymph node (LN, n = 21), peripheral blood (PB, n = 7), and bone marrow (BM, n = 3) samples from CLL patients, and reactive lymph node (rLN, n = 13) samples from heathy controls were obtained after informed consent and according to the guidelines of the Hospital Clínic Ethics Committee, the Ethics Committee of the University of Heidelberg, and the Declaration of Helsinki. Patients with CLL were diagnosed following the World Health Organization (WHO) classification criteria. All clinical information of the patients analyzed in this work is provided in Suppl. Table 1.

*Mice and tumor models*

C57BL/6 wild-type (WT) mice were purchased from Charles River Laboratories (Germany) or Janvier Labs (France). Adoptive transfer of TCL1 leukemia cells was performed as previously described (Hanna et al., 2016; Wierz et al., 2018). In short, malignant B cells were enriched from splenocytes of Eμ-TCL1 mice using EasySep Mouse Pan-B Cell Isolation Kit (StemCell Technologies, Inc., Cologne, Germany). The $CD5^+$ $CD19^+$ content of purified cells was typically above 95%, as measured by flow cytometry. 1 x $10^7$ malignant TCL1 splenocytes were transplanted by intravenous (i.v) injection into 8-12 weeks-old C57BL/6 WT female mice. Leukemia progression was monitored weekly by assessment of the percentage of $CD5^+CD19^+$ cells in the PB.

*Antibody treatments*

For Galectin-9 blockade experiments, mice were first transplanted with TCL1 leukemia cells. After 2 weeks, mice were assigned to different treatment arms according to the percentage of $CD5^+CD19^+$ (CLL) cells out of $CD45^+$ cells in PB. Subsequently, mice were injected i.p. with 6 mg/kg of anti-Galectin-9 (clone: RG9-1) or rat IgG2b isotype control antibody (clone: LTF-2), 3 times per week for another 7 weeks. All antibodies for in vivo experiments were acquired from BioXcell (West Lebanon, NH).

*Tissue sample collection and preparation of cell suspensions*

Mice were euthanized by increasing concentrations of carbon dioxide ($CO_2$) or by cervical dislocation before reaching the established humane end-point. PB was drawn from the submandibular vein or via cardiac puncture and collected in ethylenediaminetetraacetic acid (EDTA)-coated tubes (Sarstedt, Numbrecht, Germany). Single-cell suspensions from spleens, bone marrow (BM) and inguinal LNs were prepared as previously described (Hanna et al., 2016; McClanahan et al., 2015). BM cells were flushed from femurs with 5 mL of phosphate-buffered saline (PBS)/5% fetal calf serum (FCS). Spleen single-cell suspensions

were generated by using the gentleMACS tissue dissociator with Gentle MACS tubes C (Miltenyi Biotec). Single cell suspensions from LNs were prepared by grinding the tissue through 70 mm cell strainers (BD Biosciences, Heidelberg, Germany). Erythrocytes were lysed by using Red blood cell lysis buffer (Mitenyi Biotec).

*Flow cytometry*

Single-cell suspensions were immunostained with antibodies against cell surface proteins (Key Resource Table) in FACS buffer containing 0.1 % fixable viability dye (Thermo Fisher Scientific, 65- 0866-14) for 30 min at 4 °C. Cells were subsequently washed twice in FACS buffer, fixed with IC fixation buffer (Thermo Fisher Scientific, 00-8222-49) for 30 min at room temperature, washed twice with FACS buffer, and stored at 4 °C in dark conditions until being analyzed.

For transcription factor or intracellular cytokine staining, cell surface-stained cells were fixed for 30 min at room temperature with Foxp3 fixation/permeabilization buffer (Thermo Fisher Scientific, 00-5523-00 or Miltenyi Biotec, 130-093-142). After a washing step with FACS buffer, cells were permeabilized for 30 min at room temperature with 1X permeabilization buffer (Thermo Fisher Scientific, 00- 8333-56). Intracellular staining with antibodies against transcription factors or cytokines was performed in 1X permeabilization buffer for 30 min at room temperature. Excess antibodies were washed twice with 1X permeabilization buffer and cells were resuspended in 1X permeabilization buffer and stored at 4°C in dark conditions until they were analyzed by flow cytometry.

For intracellular CD107a assessment, splenocytes were stimulated overnight with phorbol myristate acetate (PMA) and ionomycin (100 nmol/L and 1 µmol/L) and incubated for 4 hours with Brefeldin A (BFA, 1X) prior to washing and cell surface staining.

Cell fluorescence was assessed using a BD LSRFortessa™ (BD Biosciences) or a Novocyte Quanteon (Agilent) flow cytometer, and data was analyzed using FlowJo X 10.0.7 software (FlowJo). In each experiment, single fluorochrome stainings were used to compensate for spectral overlap. Fluorescence minus one (FMO) controls were employed for proper gating of positive cell populations. FMO-normalized Mean Fluorescence Intensity (nMFI) for unimodal distributions or percentage of positive cells for bimodal distributions were determined for populations of interest. The standard gating strategy for analysis of CLL cells and T cells is depicted in Suppl. Figure 4A.

*Immunofluorescence of whole lymph node sections*

Paraffin-embedded tissue sections of lymph nodes were obtained from the National Center for Tumor Disease (NCT), Hospital Clínic de Barcelona, and the University of Würzburg.

After validation of primary and secondary HRP-conjugated antibodies using DAB chromogenic detection, incubation times and appropriate antibody concentrations were optimized using the Opal™ 5-color kit (Akoya Biosciences, NEL840001KT). Epitope stability was assessed to determine the order of each antibody in sequence, and antigen stripping efficiency was confirmed in all used primary antibodies.

Deparaffinization and rehydration of lymph node sections was performed by immersion in xylene for 10 minutes twice, followed by immersion in a series of descending ethanol concentrations prior to distilled water. Slides were then cooked in a steam cooker with antigen retrieval buffer pH9 (Akoya Biosciences, AR900250ML) at 100 °C for 25 minutes. Slides were allowed to cool at room temperature and washed in tris-buffered saline containing 0.1 % tween 20 (TBS-T). Next, slides were incubated with blocking buffer (Akoya Biosciences, NEL840001KT) for 10 minutes at room temperature and incubated with the primary antibody for the indicated time and concentration (Key Resource Table). After three washing steps with TBS-T, slides were incubated with anti-rabbit HRP-conjugated secondary antibody (Akoya Biosciences, NEL840001KT). Sections underwent rounds of antigen stripping via incubation at 100 °C in AR9 buffer (Akoya Biosciences, AR900250ML) for 25 minutes, allowing removal of the excess of antibody complex formed. For multi-color staining, tissue sections went through multiple rounds of blocking, primary and secondary antibody labelling, each round with a different Opal™ dye (Akoya Biosciences, NEL840001KT). Finally, background signal reduction through incubation for 10 minutes at RT in 0.1 % Sudan Black (Sigma-Aldrich, 199664) took place and sections were washed thoroughly in TBS-T. Finally, nuclei were stained with DAPI (Akoya Biosciences, NEL840001KT) and slides were mounted using ProLong Diamond Antifade Mountant (Life Technologies, P36965).
Slides were imaged using a Carl Zeiss Axioscan 7 slide scanner at 20X.

*Immunofluorescence staining and imaging of CLL TMA*

TMA 159/2 was de-paraffinized and subjected to antigen retrieval for 5 minutes at 95°C followed by 5 minutes at 107°C, using pH8.5 EZ-AR 2 Elegance buffer (BioGenex). To reduce tissue autofluorescence, slides were placed in a transparent reservoir containing 4.5% $H_2O_2$ and 24 mM NaOH in PBS and illuminated with white light for 60 minutes followed by 365 nm light for 30 minutes at room temperature as previously described (Lin et al., 2018). Slides were rinsed with surfactant wash buffer (0.025% Triton X-100 in PBS), placed in a humidified stain tray, and incubated in Image-iT™ FX Signal Enhancer (Thermo Fisher) for 15 minutes at room temperature. After rinsing with surfactant wash buffer, the slides were placed in a humidity tray and stained with the panel of fluor- and hapten-labeled primary antibodies in PBS-Antibody Stabilizer (CANDOR Bioscience GmbH) containing 5% mouse serum and 5% rabbit serum for 2 hours at room temperature. Slides were then rinsed again

with surfactant wash buffer and placed in a humidified stain tray and incubated with SYTOX Blue (Thermo Fisher), ArgoFluor™ 845 mouse-anti-DIG in PBS-Antibody Stabilizer containing 10% goat serum for 30 minutes at room temperature. The slides were then rinsed a final time with surfactant wash buffer and PBS, coverslipped with ArgoFluor™ Mounting Media (RareCyte, Inc.) and dried overnight (Lin et al., 2022).

Slides were imaged using an Orion instrument (RareCyte, Inc.) at 20X. Raw image files were processed to correct for system aberrations; then signals from individual targets were isolated to separate channels using the Spectral Matrix obtained with control samples, followed by stitching of FOVs to generate a continuous open microscopy environment (OME) pyramid TIFF image.

*Image analysis*

Preprocessing

TMA 159/2 with 18-color staining was analyzed using the multiple-choice microscopy pipeline MCMICRO (Schapiro et al., 2022) (Commit 91fcd5eefd69da112414b06cf3a65a9a66afeccf). Dearraying was performed by Coreograph (Schapiro et al., 2022) 2.2.8, Unmicst (Yapp et al., 2022) 2.7.0 segmented the cells based on the nuclear channel Sytox, S3segmenter (Saka et al., 2019) 1.3.12 generated single-cell masks and Mcquant (Schapiro et al., 2022) 1.5.1 quantified the signal of each of the 18 channels in each cell. The corresponding parameters (params.yml) for full reproducibility of this MCMICRO runs are available on Github (https://github.com/SchapiroLabor/ImageAnalysisTMA159_2).

Following visual inspection of Coreograph's QC file, all cores that were damaged were filtered out. Additionally, the 4 muscle tissue cores – which were used as control – were filtered. In total we performed the downstream analysis with 42 cores. Channel numbers 2 (Sytox), 14 (E-cadherin), 17 (Pan-CK) and 18 (AF-Tissue) were removed for downstream analysis since (i) Sytox and AF-Tissue represent nuclei and autofluorescence which are not relevant for cell type calling; and (ii) E-cadherin and Pan-CK expression are not expected in LN tissue and therefore, failed our visual QC due to unspecific staining patterns. Image visualization was performed with QuPath (Bankhead et al., 2017) and Napari (Chiu et al., 2022).

Batch correction

Cell type clustering on the raw data results in clusters consisting mainly of cells of a single core of origin. This is due to preanalytical variability, which requires batch correction on core-level. Therefore, marker intensities were normalized with Mxnorm (Harris et al., 2022)

0.0.0.9000 (transform: log10_mean_divide, method: none) before using Rphenograph (Levine et al., 2015) 0.99.1 to cluster the individual cell types.

Cell type assignment

Cell types were assigned based on marker thresholding (positive / negative) and comparison to an expert curated list of markers associated with the specific cell types (Suppl. Table 2).

Spatial Analysis

Neighborhood analysis was performed with Giotto 1.1.2 (Dries et al., 2021). After building a Delaunay network and running 1000 simulations, we compared the number of observed interactions between the cell types with their respective expected number of interactions. Cell-cell interactions between the same cell types are significantly enriched because of segmentation inaccuracies. Cells are slightly over segmented creating multiple cells with the same phenotype.

Statistical analysis

The subsequently calculated cell type frequencies in each core were used to perform two-sided t-tests (base package stats) for changes in cell type frequencies between patients that were positive or negative for a variety of binary clinical parameters (sex, IGHV, del13q, del17p, died, treated, del17p_tp53 (del17p and/or tp53 positive)). Additionally, Cox regression (survivalAnalysis 0.3.0) was calculated on overall survival and time to next treatment. Finally, correlation with the Pearson method was checked (cor.test() in base package stats) between overall survival, time to next treatment and all cell type frequencies.
Up to the statistical analysis, calculations were performed under R version 4.1.0 (2021-05-18) on platform x86_64-apple-darwin17.0 (64-bit) running under macOS 13.0. Statistical analysis was done on R version 4.0.5 (2021-03-31) on platform: x86_64-apple-darwin17.0 (64-bit) running under: macOS Big Sur 10.16.
All mentioned steps of image processing were performed on the BWforCluster.

*Mass cytometry*

A panel of 42 heavy metal-labeled antibodies for detection of both surface and intracellular proteins was adopted from Bengsch et al. and modified based on literature research in order to characterize diverse T cell phenotypes (Bengsch et al., 2018). The complete list of proteins detected and the heavy metal-conjugated antibodies used are listed in the Key Resource Table. For most of the markers, heavy metal-conjugated antibodies were commercially available and purchased from Fluidigm. Where no heavy metal-

conjugated antibodies were commercially available, coupling of heavy metal to respective antibodies was performed in-house using the Maxpar® X8 Multimetal Labeling kit (Fluidigm) following the manufacturer's instructions. $^{113}$In, $^{115}$In and $^{139}$La heavy metal isotopes (#) were not available from Fluidigm and were purchased from Trace Sciences International ($^{113}$In) and Sigma ($^{115}$In, #203440-1G; $^{139}$La, #211605-100G) Following the preparation of a 1M solution, $^{113}$In, $^{115}$Ln and $^{139}$La heavy-metal isotopes (#) were conjugated to monoclonal purified IgG antibodies using the Maxpar® X8 Multimetal Labeling kit (Fluidigm, #201300).

Frozen cell suspensions were thawed and washed prior to incubation in 15 mL of pre-heated RPMI 1640 containing 10 % FBS in a roller incubator for 30 min at room temperature. Cells were filtered to remove dead cells and B-cell depletion was performed using human CD19 microbead (Miltenyi Biotec) labeling according to the manufacturer's protocol. Unlabeled CD19$^-$ cells were collected, washed, filtered, and counted prior to mass cytometry processing.

CD19-depleted single-cell suspensions were stained as previously described (Wierz et al., 2018). Briefly, cells were stained with 5 µM cisplatin (Cell-ID Cisplatin, Fluidigm) for 5 min in order to label dead cells. Cells were then washed once and cell surface staining was performed for 30 min at room temperature. After a washing step, cells were fixed with Fixation/Permeabilization buffer (Thermo Fisher Scientific) following the manufacturer's instructions. Intracellular staining was performed by incubating the antibody- cocktail for 30 min at room temperature. After a washing step, cells were stained with cell-ID Intercalator-Ir (Fluidigm) in fixation and permeabilization solution, followed by another two washing steps with PBS and dd$H_2O$, respectively. Prior to acquisition, cells were resuspended at a concentration of 5 x $10^5$ cells/mL in dd$H_2O$ with 1:10 calibration beads (EQ Four Element Calibration Beads, Fluidigm). Samples were analyzed at a flow rate of 0.03 mL/min with the Helios mass cytometer (Fluidigm) of the National Cytometry Platform (LIH). Initial data processing and quality control were performed. Flow cytometry standard (FCS) files were normalized with EQ beads using the HELIOS instrument acquisition software (Fluidigm).

As a first analysis step, samples were pre-gated as follows: gates were placed on cells (Beads vs. Ir191), singlets (Ir193 vs. Ir191) and live cells (Pt195$^-$). Next, non-B immune cells (CD19$^-$ CD45$^+$) and CD3$^+$ T cells (CD3$^+$ NCAM$^-$) were selected exported as .fcs files.

Raw data .fcs files were merged into a flowSet object using flowCore package (Hahne et al., 2009). Signal intensities for each marker were arcsinh-transformed using a co-factor of 5 (default) (Bruggner et al., 2014). Sample quality was assessed based on cell counts per sample and samples with less than 1,500 cells were excluded. Multi-dimension scaling (MDS) plotting using median arcsinh-transformed marker expression for all cells in each sample was used for sample clustering analysis.

Cytometry data analysis tools (CATALYST) R package (Chevrier et al., 2018) containing FlowSOM (Van Gassen et al., 2015) and ConsensusClusterPlus (Wilkerson and Hayes, 2010) metaclustering methods was used for cell cluster identification using all cells from all samples. Clustering was performed using arcsinh-transformed expression of 33 markers, i.e., excluding the markers DNA content and cisplatin viability, which were used to select viable, single cells, and CD19 and HLA-DR, which were used to exclude B cells (Key Resource Table). TIM3, LAG3, GITR, CD47 and 4-1BB were excluded from the analysis due to low signal and likely adding noise in the cluster generation process.

The maximum number of clusters allowed to be evaluated was set to maxK = 30, after biological relevance of obtained clusters was assessed, and $k < 30$ and $k > 30$ were verified to be underfitting or overfitting, respectively. Cell clustering was visualized using the UMAP algorithm, displaying 1 $x10^3$ random cells from each sample. The robustness of this approach was evaluated by repeatedly plotting an increasing number of randomly picked cells from each sample, with a range of 200 to 1,000 cells, and evaluating the similarity of the 30 subpopulations recognized in the respective UMAP plots. Sample #HD3 was excluded as an outlier.

*Cell sorting for single-cell RNA and TCR sequencing*

Single-cell suspensions from LNs of CLL patients were retrieved by partially thawing vials of cryopreserved cells in order to preserve unused cells. Samples were stained for cell surface proteins for 30 min. After washing with PBS, cells were resuspended in PBS + 5 % FBS containing 0.2 µg/mL DAPI prior cell sorting. The gating strategy for $CD3^+$ T cell and CLL cell sorting is depicted in Suppl. Figure 5A. Cells were sorted in PBS + 2 % FBS using a BD FACSAria™ II or BD FACSArisa Fusion (both from BD Biosciences) cell sorters. The purity of cells after sorting was above 95 %.

*Single-cell RNA sequencing library construction using the 10x Genomics Chromium platform*

Five CLL LN samples were processed for single-cell TCR and 5' gene expression profiling of CD3 T cells and CLL cells using the Chromium Next GEM Single Cell V(D)J Solution from 10x Genomics following the manufacturer's instructions. Briefly, for a target cell recovery of 5,000 cells, the concentration of T cells was adjusted to 1 $x10^3$ cells/µL and tumor cells were added at a ratio of 1:20. Cells were then loaded into the Single Cell A Chip (10x Genomics). GEX libraries were sequenced on a HiSeq 4000 machine (Illumina) or on a NovaSeq 6000 (Illumina), and V(D)J-enriched libraries were sequenced on a NextSeq 550 (Illumina).

*Single cell RNA-Seq data processing*

Sequencing reads were aligned by Cell Ranger (5.0.1) to reference version hg38(2020-A) for human data and to reference version mm10(2020-A) for mouse data. Raw count matrices were processed by the quality control pipeline to determine the optimal cut-offs for filtering. Cells were filtered by read counts and mitochondrial RNA content. Lower cut-off for read counts were determined by read-counts distribution for samples in each dataset and were set at 350 for human and 500 for mouse, mitochondrial RNA content should be lower than 10%.

Raw gene count matrices were processed by Seurat(v4.1.0) (Hao et al., 2021), expression values were normalized and scaled by SCTransform. Doublets were filtered by DoubletFinder(2.0.3) (McGinnis et al., 2019). Dimensional reduction was performed by Principle Component Analysis (PCA). Datasets were integrated by HARMONY (Korsunsky et al., 2019) to reduce batch bias on calculated principal components. Sample identity was used as the batch variable for HARMONY integration. Uniform Manifold Approximation and Projection (UMAP) was used for dimensional reduction on first 23 HARMONY computed cell-embeddings.

Cluster were defined by the Louvain method at the resolution of 0.5, clusters defined at this step were used for annotation by manual curation. Markers for each cluster were produced by differential expression analysis searching for overexpressing markers of each cluster. Top 10 overexpressing markers of each cluster were illustrated by a heatmap. To reveal potential substructure among cell types of interest, we performed a subcluster analysis on the $T_{FH}$ cluster. UMAP analysis was repeated on the harmony corrected embeddings of cells from the $T_{FH}$ cluster to reveal substructures.

*Pseudotime analysis*

Diffusion pseudotime analysis was performed using destiny(3.8.1) (Angerer et al., 2016). Cells expressing CD4 and CD8 were analysed separately. To retrieve the pseudotime of each marker differentiated cell groups, “DPT” function from destiny was used for computing the diffusion pseudotime on each cell. For each cell type, the root nodes were placed within the corresponding naïve cell type cluster.

To performed differential gene expression analysis on pseudotime, the diffusion pseudotime values of cells in trajectories were analysed together with their transcript expression values by tradeSeq (Van den Berge et al., 2020). Differentially expressed genes were plotted against ranked diffusion pseudotime for illustration.

*TCR data analysis*

V(D)J transcripts from single cells were aligned and counted using the Cell Ranger pipeline (5.0.1). GRCm38 VDJ Reference 5.0.0 from 10X genomics was used for mouse

data and GRCh38 VDJ Reference 5.0.0 from 10X genomics was used for human data. In addition, an output file containing TCR α- and β-chain CDR3 nucleotide sequences and a cell barcode for all single cells was generated. Only productive rearrangements were evaluated, and 3 or more cells containing the same α- and β-chain CDR3 consensus nucleotide sequences were considered cell clones. scRepertoire (Borcherding et al., 2020) was used to process contig and clonotype information from Cell Ranger. The summarized TCR information per cell was merged with Seurat object using the shared cell barcodes between the TCR library and the RNA-Seq library for integrated analysis. Shannon diversity index was computed to represent the diversity of the TCR repertoire in each single cell clusters. Cells with expanded TCRs are categorized by their expansion level and then illustrated by umap plots. To illustrate expanded TCRs shared between different clusters, cells with expanded TCRs were represented by two types of chord diagrams. The first type depicts how other clusters share expanded TCRs with CD8 TEM clusters, where a chord diagram was created for each CD8 TEM cluster. Circular fragments in these chord diagrams represent cells carrying an expanded TCR in each cell type, arcs connect cells that share the same TCRs with the CD8 TEM of interest. Width of the arcs is scaled by the number of cells sharing same TCRs. The second type of chord diagram present a similar concept, it depicts TCR sharing across all cell types instead of one.

The VDJdb browser (Bagaev et al., 2020) was used in order to identify CDR3 regions from the V(D)J single-cell dataset whose antigen-specificity has been reported. Both TCR α- and β- chain CDR3 amino acid sequences from each sample were used for the literature analysis aimed at identifying previously described binding epitopes.

*Ligand-receptor interaction analysis*

To find differential ligand-receptor interactions between datasets, a control dataset derived from 5 reactive lymph nodes (Aoki et al., 2020) was added for comparison. The reactive lymph node dataset was independently processed by the same quality control pipeline and single cell analysis pipeline. CellChat was used for differential cell-cell communication analysis. Ligand-receptor interactions from OmnipathR database (Türei et al., 2021) were included as candidates. CellChat analysis was first performed independently on the two datasets using LIANA (Dimitrov et al., 2022). The results were then contrasted by CellChat for differential interactions. Labels from the two comparing datasets were harmonized to 8 major cell types (CLL/B, CD4 $T_{CM}$, $T_{REG}$, CD4 $T_{EM}$, CD8 $T_{EM}$, CD4 $T_N$, CD8 $T_N$, $T_{FH}$) for comparison. Differential Interactions with p-values below 0.01 were visualized by the dot plot functions of CellChat.

*Expression of Galectin-9 protein and its impact on survival in CLL*

Galectin-9 protein levels in CLL patient samples were obtained from Herbst SA, Vesterlund M, *et al.* (Herbst et al., 2022). Mean relative Galectin-9 levels were compared between IGHV-mutated and -unmutated CLL patients using a two-sided Wilcoxon signed-rank test. Time to next treatment (TTNT) was calculated from the date of sample collection to subsequent treatment initiation. Proportional hazards regression (Cox regression) was used to calculate the impact of Galectin-9 abundance on TTNT using the R package survival (version 3.2-3). Kaplan-Meier curves were plotted for all samples and for IGHV-mutated and -unmutated CLL patients separately.

*Expression of LGALS9 and its impact on survival in TCGA samples*

Expression of *LGALS9* in TCGA samples was gathered with R (4.3.1) and Bioconductor using library RTCGA.rnaseq (1.3.0,2015-11-01) and RTCGA.clinical (1.3.0,2015-11-01). Survival curves were prepared by survminer (0.4.9) splitting the samples based on the median *LGALS9* expression into two groups. Differences in survival were assessed using Cox proportional hazard model and multiple testing was corrected according to Benjamini Hochberg. GEPIA2 was used to compare tumor and normal samples from TCGA and the GTEx projects, using a standard processing pipeline (Tang et al., 2019).

*Expression of LGALS9 in single-cell RNAseq data sets*

The expression of *LGALS9* was assessed in renal cell carcinoma (SCP1288) (Bi et al., 2021) and glioblastoma (SCP1985) (Abdelfattah et al., 2022). Data was collected from (https://singlecell.broadinstitute.org/single_cell) and processed in R using Seurat (4.9.9.9044). In short, data was loaded using Read10X and after the creation of a Seurat object (min.cells=3, min.features=200) processed using default values with NormalizeData, FindVariableFeatures, ScaleData, RunPCA, FindNeighbours, FindClusters, and RunTSNE. Figures were prepared using FeaturePlot and DimPlot highlighting cell types. Violin plots were prepared using ggplot2 (3.4.2).

**Data availability**

Human single-cell RNA- and TCR-sequencing data are deposited to European Genome-phenome Archive (EGA) under the accession ID (Pending) and are available on request. Mouse single-cell RNA- and TCR-sequencing data are available on Gene Expression Omnibus under the accession ID (Pending).

## References


Abdelfattah, N., P. Kumar, C. Wang, J.S. Leu, W.F. Flynn, R. Gao, D.S. Baskin, K. Pichumani, O.B. Ijare, S.L. Wood, S.Z. Powell, D.L. Haviland, B.C. Parker Kerrigan, F.F. Lang, S.S. Prabhu, K.M. Huntoon, W. Jiang, B.Y.S. Kim, J. George, and K. Yun. 2022. Single-cell analysis of human glioma and immune cells identifies S100A4 as an immunotherapy target. *Nat Commun*. 13:767.

Andreatta, M., J. Corria-Osorio, S. Müller, R. Cubas, G. Coukos, and S.J. Carmona. 2021. Interpretation of T cell states from single-cell transcriptomics data using reference atlases. *Nat Commun*. 12:2965.

Angerer, P., L. Haghverdi, M. Büttner, F.J. Theis, C. Marr, and F. Buettner. 2016. destiny: diffusion maps for large-scale single-cell data in R. *Bioinformatics*. 32:1241-1243.

Aoki, T., L.C. Chong, K. Takata, K. Milne, M. Hav, A. Colombo, E.A. Chavez, M. Nissen, X. Wang, T. Miyata-Takata, V. Lam, E. Viganò, B.W. Woolcock, A. Telenius, M.Y. Li, S. Healy, C. Ghesquiere, D. Kos, T. Goodyear, J. Veldman, A.W. Zhang, J. Kim, S. Saberi, J. Ding, P. Farinha, A.P. Weng, K.J. Savage, D.W. Scott, G. Krystal, B.H. Nelson, A. Mottok, A. Merchant, S.P. Shah, and C. Steidl. 2020. Single-Cell Transcriptome Analysis Reveals Disease-Defining T-cell Subsets in the Tumor Microenvironment of Classic Hodgkin Lymphoma. *Cancer discovery*. 10:406-421.

Bagaev, D.V., R.M.A. Vroomans, J. Samir, U. Stervbo, C. Rius, G. Dolton, A. Greenshields-Watson, M. Attaf, E.S. Egorov, I.V. Zvyagin, N. Babel, D.K. Cole, A.J. Godkin, A.K. Sewell, C. Kesmir, D.M. Chudakov, F. Luciani, and M. Shugay. 2020. VDJdb in 2019: database extension, new analysis infrastructure and a T-cell receptor motif compendium. *Nucleic Acids Res*. 48:D1057-d1062.

Bankhead, P., M.B. Loughrey, J.A. Fernández, Y. Dombrowski, D.G. McArt, P.D. Dunne, S. McQuaid, R.T. Gray, L.J. Murray, H.G. Coleman, J.A. James, M. Salto-Tellez, and P.W. Hamilton. 2017. QuPath: Open source software for digital pathology image analysis. *Sci Rep*. 7:16878.

Bengsch, B., T. Ohtani, O. Khan, M. Setty, S. Manne, S. O'Brien, P.F. Gherardini, R.S. Herati, A.C. Huang, K.M. Chang, E.W. Newell, N. Bovenschen, D. Pe'er, S.M. Albelda, and E.J. Wherry. 2018. Epigenomic-Guided Mass Cytometry Profiling Reveals Disease-Specific Features of Exhausted CD8 T Cells. *Immunity*. 48:1029-1045.e1025.

Bi, K., M.X. He, Z. Bakouny, A. Kanodia, S. Napolitano, J. Wu, G. Grimaldi, D.A. Braun, M.S. Cuoco, A. Mayorga, L. DelloStritto, G. Bouchard, J. Steinharter, A.K. Tewari, N.I. Vokes, E. Shannon, M. Sun, J. Park, S.L. Chang, B.A. McGregor, R. Haq, T. Denize, S. Signoretti, J.L. Guerriero, S. Vigneau, O. Rozenblatt-Rosen, A. Rotem, A. Regev, T.K. Choueiri, and E.M. Van Allen. 2021. Tumor and immune reprogramming during immunotherapy in advanced renal cell carcinoma. *Cancer cell*. 39:649-661.e645.

Bichi, R., S.A. Shinton, E.S. Martin, A. Koval, G.A. Calin, R. Cesari, G. Russo, R.R. Hardy, and C.M. Croce. 2002. Human chronic lymphocytic leukemia modeled in mouse by targeted TCL1 expression. *Proc Natl Acad Sci U S A*. 99:6955-6960.

Blank, C.U., W.N. Haining, W. Held, P.G. Hogan, A. Kallies, E. Lugli, R.C. Lynn, M. Philip, A. Rao, N.P. Restifo, A. Schietinger, T.N. Schumacher, P.L. Schwartzberg, A.H. Sharpe, D.E. Speiser, E.J. Wherry, B.A. Youngblood, and D. Zehn. 2019. Defining 'T cell exhaustion'. *Nat Rev Immunol*. 19:665-674.

Borcherding, N., N.L. Bormann, and G. Kraus. 2020. scRepertoire: An R-based toolkit for single-cell immune receptor analysis. *F1000Res*. 9:47.

Bruggner, R.V., B. Bodenmiller, D.L. Dill, R.J. Tibshirani, and G.P. Nolan. 2014. Automated identification of stratifying signatures in cellular subpopulations. *Proc Natl Acad Sci U S A*. 111:E2770-2777.

Burger, J.A., M.P. Quiroga, E. Hartmann, A. Bürkle, W.G. Wierda, M.J. Keating, and A. Rosenwald. 2009. High-level expression of the T-cell chemokines CCL3 and CCL4 by chronic lymphocytic leukemia B cells in nurselike cell cocultures and after BCR stimulation. *Blood*. 113:3050-3058.

Buschle, M., D. Campana, S.R. Carding, C. Richard, A.V. Hoffbrand, and M.K. Brenner. 1993. Interferon gamma inhibits apoptotic cell death in B cell chronic lymphocytic leukemia. *J Exp Med*. 177:213-218.

Cappell, K.M., R.M. Sherry, J.C. Yang, S.L. Goff, D.A. Vanasse, L. McIntyre, S.A. Rosenberg, and J.N. Kochenderfer. 2020. Long-Term Follow-Up of Anti-CD19 Chimeric Antigen Receptor T-Cell Therapy. *J Clin Oncol*. 38:3805-3815.

Chevrier, D.M., L. Raich, C. Rovira, A. Das, Z. Luo, Q. Yao, A. Chatt, J. Xie, R. Jin, J. Akola, and P. Zhang. 2018. Molecular-Scale Ligand Effects in Small Gold-Thiolate Nanoclusters. *J Am Chem Soc*. 140:15430-15436.

Chiu, C.-L., N. Clack, and t.n. community. 2022. napari: a Python Multi-Dimensional Image Viewer Platform for the Research Community. *Microscopy and Microanalysis*. 28:1576-1577.

Connolly, K.A., M. Kuchroo, A. Venkat, A. Khatun, J. Wang, I. William, N.I. Hornick, B.L. Fitzgerald, M. Damo, M.Y. Kasmani, C. Cui, E. Fagerberg, I. Monroy, A. Hutchins, J.F. Cheung, G.G. Foster, D.L. Mariuzza, M. Nader, H. Zhao, W. Cui, S. Krishnaswamy, and N.S. Joshi. 2021. A reservoir of stem-like CD8(+) T cells in the tumor-draining lymph node preserves the ongoing antitumor immune response. *Science immunology*. 6:eabg7836.

Curigliano, G., H. Gelderblom, N. Mach, T. Doi, D. Tai, P.M. Forde, J. Sarantopoulos, P.L. Bedard, C.C. Lin, F.S. Hodi, S. Wilgenhof, A. Santoro, C.A. Sabatos-Peyton, T.A. Longmire, A. Xyrafas, H. Sun, S. Gutzwiller, L. Manenti, and A. Naing. 2021. Phase I/Ib Clinical Trial of Sabatolimab, an Anti-TIM-3 Antibody, Alone and in Combination with Spartalizumab, an Anti-PD-1 Antibody, in Advanced Solid Tumors. *Clin Cancer Res*. 27:3620-3629.

Daley, D., V.R. Mani, N. Mohan, N. Akkad, A. Ochi, D.W. Heindel, K.B. Lee, C.P. Zambirinis, G.S.B. Pandian, S. Savadkar, A. Torres-Hernandez, S. Nayak, D. Wang, M. Hundeyin, B. Diskin, B. Aykut, G. Werba, R.M. Barilla, R. Rodriguez, S. Chang, L. Gardner, L.K. Mahal, B. Ueberheide, and G. Miller. 2017. Dectin 1 activation on macrophages by galectin 9 promotes pancreatic carcinoma and peritumoral immune tolerance. *Nat Med*. 23:556-567.

Damle, R.N., T. Wasil, F. Fais, F. Ghiotto, A. Valetto, S.L. Allen, A. Buchbinder, D. Budman, K. Dittmar, J. Kolitz, S.M. Lichtman, P. Schulman, V.P. Vinciguerra, K.R. Rai, M. Ferrarini, and N. Chiorazzi. 1999. Ig V gene mutation status and CD38 expression as novel prognostic indicators in chronic lymphocytic leukemia. *Blood*. 94:1840-1847.

de Mingo Pulido, Á., A. Gardner, S. Hiebler, H. Soliman, H.S. Rugo, M.F. Krummel, L.M. Coussens, and B. Ruffell. 2018. TIM-3 Regulates $CD103^{+}$ Dendritic Cell Function and Response to Chemotherapy in Breast Cancer. *Cancer cell*. 33:60-74.e66.

Dimitrov, D., D. Türei, M. Garrido-Rodriguez, P.L. Burmedi, J.S. Nagai, C. Boys, R.O. Ramirez Flores, H. Kim, B. Szalai, I.G. Costa, A. Valdeolivas, A. Dugourd, and J. Saez-Rodriguez. 2022. Comparison of methods and resources for cell-cell communication inference from single-cell RNA-Seq data. *Nat Commun*. 13:3224.

Ding, W., B.R. LaPlant, T.G. Call, S.A. Parikh, J.F. Leis, R. He, T.D. Shanafelt, S. Sinha, J. Le-Rademacher, A.L. Feldman, T.M. Habermann, T.E. Witzig, G.A. Wiseman, Y. Lin, E. Asmus, G.S. Nowakowski, M.J. Conte, D.A. Bowen, C.N. Aitken, D.L. Van Dyke, P.T. Greipp, X. Liu, X. Wu, H. Zhang, C.R. Secreto, S. Tian, E. Braggio, L.E. Wellik, I. Micallef, D.S. Viswanatha, H. Yan, A.A. Chanan-Khan, N.E. Kay, H. Dong, and S.M. Ansell. 2017. Pembrolizumab in patients with CLL and Richter transformation or with relapsed CLL. *Blood*. 129:3419-3427.

Dries, R., Q. Zhu, R. Dong, C.L. Eng, H. Li, K. Liu, Y. Fu, T. Zhao, A. Sarkar, F. Bao, R.E. George, N. Pierson, L. Cai, and G.C. Yuan. 2021. Giotto: a toolbox for integrative analysis and visualization of spatial expression data. *Genome Biol*. 22:78.

Fraietta, J.A., S.F. Lacey, E.J. Orlando, I. Pruteanu-Malinici, M. Gohil, S. Lundh, A.C. Boesteanu, Y. Wang, R.S. O'Connor, W.-T. Hwang, E. Pequignot, D.E. Ambrose, C. Zhang, N. Wilcox, F. Bedoya, C. Dorfmeier, F. Chen, L. Tian, H. Parakandi, M. Gupta, R.M. Young, F.B. Johnson, I. Kulikovskaya, L. Liu, J. Xu, S.H. Kassim, M.M. Davis, B.L. Levine, N.V. Frey, D.L. Siegel, A.C. Huang, E.J. Wherry, H. Bitter, J.L.

Brogdon, D.L. Porter, C.H. June, and J.J. Melenhorst. 2018. Determinants of response and resistance to CD19 chimeric antigen receptor (CAR) T cell therapy of chronic lymphocytic leukemia. *Nat Med*. 24:563-571.

Guo, X., Y. Zhang, L. Zheng, C. Zheng, J. Song, Q. Zhang, B. Kang, Z. Liu, L. Jin, R. Xing, R. Gao, L. Zhang, M. Dong, X. Hu, X. Ren, D. Kirchhoff, H.G. Roider, T. Yan, and Z. Zhang. 2018. Global characterization of T cells in non-small-cell lung cancer by single-cell sequencing. *Nat Med*. 24:978-985.

Gupta, S., R. Bi, K. Su, L. Yel, S. Chiplunkar, and S. Gollapudi. 2004. Characterization of naïve, memory and effector CD8+ T cells: effect of age. *Exp Gerontol*. 39:545-550.

Hahne, F., N. LeMeur, R.R. Brinkman, B. Ellis, P. Haaland, D. Sarkar, J. Spidlen, E. Strain, and R. Gentleman. 2009. flowCore: a Bioconductor package for high throughput flow cytometry. *BMC Bioinformatics*. 10:106.

Hamblin, T.J., Z. Davis, A. Gardiner, D.G. Oscier, and F.K. Stevenson. 1999. Unmutated Ig V(H) genes are associated with a more aggressive form of chronic lymphocytic leukemia. *Blood*. 94:1848-1854.

Hanna, B.S., L. Llaó-Cid, M. Iskar, P.M. Roessner, L.C. Klett, J.K.L. Wong, Y. Paul, N. Ioannou, S. Öztürk, N. Mack, V. Kalter, D. Colomer, E. Campo, J. Bloehdorn, S. Stilgenbauer, S. Dietrich, M. Schmidt, R. Gabriel, K. Rippe, M. Feuerer, A.G. Ramsay, P. Lichter, M. Zapatka, and M. Seiffert. 2021. Interleukin-10 receptor signaling promotes the maintenance of a PD-1(int) TCF-1(+) CD8(+) T cell population that sustains anti-tumor immunity. *Immunity*. 54:2825-2841.e2810.

Hanna, B.S., F. McClanahan, H. Yazdanparast, N. Zaborsky, V. Kalter, P.M. Rößner, A. Benner, C. Dürr, A. Egle, J.G. Gribben, P. Lichter, and M. Seiffert. 2016. Depletion of CLL-associated patrolling monocytes and macrophages controls disease development and repairs immune dysfunction in vivo. *Leukemia*. 30:570-579.

Hanna, B.S., S. Öztürk, and M. Seiffert. 2019. Beyond bystanders: Myeloid cells in chronic lymphocytic leukemia. *Molecular Immunology*. 110:77-87.

Hao, Y., S. Hao, E. Andersen-Nissen, W.M. Mauck, 3rd, S. Zheng, A. Butler, M.J. Lee, A.J. Wilk, C. Darby, M. Zager, P. Hoffman, M. Stoeckius, E. Papalexi, E.P. Mimitou, J. Jain, A. Srivastava, T. Stuart, L.M. Fleming, B. Yeung, A.J. Rogers, J.M. McElrath, C.A. Blish, R. Gottardo, P. Smibert, and R. Satija. 2021. Integrated analysis of multimodal single-cell data. *Cell*. 184:3573-3587.e3529.

Harris, C.R., E.T. McKinley, J.T. Roland, Q. Liu, M.J. Shrubsole, K.S. Lau, R.J. Coffey, J. Wrobel, and S.N. Vandekar. 2022. Quantifying and correcting slide-to-slide variation in multiplexed immunofluorescence images. *Bioinformatics*. 38:1700-1707.

Herbst, S.A., M. Vesterlund, A.J. Helmboldt, R. Jafari, I. Siavelis, M. Stahl, E.C. Schitter, N. Liebers, B.J. Brinkmann, F. Czernilofsky, T. Roider, P.M. Bruch, M. Iskar, A. Kittai, Y. Huang, J. Lu, S. Richter, G. Mermelekas, H.M. Umer, M. Knoll, C. Kolb, A. Lenze, X. Cao, C. Österholm, L. Wahnschaffe, C. Herling, S. Scheinost, M. Ganzinger, L. Mansouri, K. Kriegsmann, M. Kriegsmann, S. Anders, M. Zapatka, G. Del Poeta, A. Zucchetto, R. Bomben, V. Gattei, P. Dreger, J. Woyach, M. Herling, C. Müller-Tidow, R. Rosenquist, S. Stilgenbauer, T. Zenz, W. Huber, E. Tausch, J. Lehtiö, and S. Dietrich. 2022. Proteogenomics refines the molecular classification of chronic lymphocytic leukemia. *Nat Commun*. 13:6226.

Huang, Q., X. Wu, Z. Wang, X. Chen, L. Wang, Y. Lu, D. Xiong, Q. Liu, Y. Tian, H. Lin, J. Guo, S. Wen, W. Dong, X. Yang, Y. Yuan, Z. Yue, S. Lei, Q. Wu, L. Ran, L. Xie, Y. Wang, L. Gao, Q. Tian, X. Zhou, B. Sun, L. Xu, Z. Tang, and L. Ye. 2022. The primordial differentiation of tumor-specific memory CD8(+) T cells as bona fide responders to PD-1/PD-L1 blockade in draining lymph nodes. *Cell*. 185:4049-4066.e4025.

Im, S.J., M. Hashimoto, M.Y. Gerner, J. Lee, H.T. Kissick, M.C. Burger, Q. Shan, J.S. Hale, J. Lee, T.H. Nasti, A.H. Sharpe, G.J. Freeman, R.N. Germain, H.I. Nakaya, H.-H. Xue, and R. Ahmed. 2016. Defining CD8+ T cells that provide the proliferative burst after PD-1 therapy. *Nature*. 537:417.

Jikuya, R., T. Kishida, M. Sakaguchi, T. Yokose, M. Yasui, A. Hashizume, T. Tatenuma, N. Mizuno, K. Muraoka, S. Umemoto, M. Kawai, M. Yoshihara, Y. Nakamura, Y. Miyagi,

and T. Sasada. 2020. Galectin-9 expression as a poor prognostic factor in patients with renal cell carcinoma. *Cancer Immunology, Immunotherapy*. 69:2041-2051.

Jin, S., C.F. Guerrero-Juarez, L. Zhang, I. Chang, R. Ramos, C.H. Kuan, P. Myung, M.V. Plikus, and Q. Nie. 2021. Inference and analysis of cell-cell communication using CellChat. *Nat Commun*. 12:1088.

Jitschin, R., M. Braun, M. Büttner, K. Dettmer-Wilde, J. Bricks, J. Berger, M.J. Eckart, S.W. Krause, P.J. Oefner, K. Le Blanc, A. Mackensen, and D. Mougiakakos. 2014. CLL-cells induce IDOhi CD14+HLA-DRlo myeloid-derived suppressor cells that inhibit T-cell responses and promote TRegs. *Blood*. 124:750-760.

Joshi, N.S., W. Cui, A. Chandele, H.K. Lee, D.R. Urso, J. Hagman, L. Gapin, and S.M. Kaech. 2007. Inflammation directs memory precursor and short-lived effector CD8(+) T cell fates via the graded expression of T-bet transcription factor. *Immunity*. 27:281-295.

Kallies, A., D. Zehn, and D.T. Utzschneider. 2020. Precursor exhausted T cells: key to successful immunotherapy? *Nat Rev Immunol*. 20:128-136.

Karabon, L., A. Partyka, L. Ciszak, E. Pawlak-Adamska, A. Tomkiewicz, A. Bojarska-Junak, J. Roliński, D. Wołowiec, T. Wrobel, I. Frydecka, and A. Kosmaczewska. 2020. Abnormal Expression of BTLA and CTLA-4 Immune Checkpoint Molecules in Chronic Lymphocytic Leukemia Patients. *J Immunol Res*. 2020:6545921.

Kiaii, S., P. Kokhaei, F. Mozaffari, E. Rossmann, F. Pak, A. Moshfegh, M. Palma, L. Hansson, K. Mashayekhi, M. Hojjat-Farsangi, A. Österborg, A. Choudhury, and H. Mellstedt. 2013. T cells from indolent CLL patients prevent apoptosis of leukemic B cells in vitro and have altered gene expression profile. *Cancer immunology, immunotherapy : CII*. 62:51-63.

Korsunsky, I., N. Millard, J. Fan, K. Slowikowski, F. Zhang, K. Wei, Y. Baglaenko, M. Brenner, P.R. Loh, and S. Raychaudhuri. 2019. Fast, sensitive and accurate integration of single-cell data with Harmony. *Nat Methods*. 16:1289-1296.

Lee, M., J.A.G. Hamilton, G.R. Talekar, A.J. Ross, L. Michael, M. Rupji, B. Dwivedi, S.S. Raikar, J. Boss, C.D. Scharer, D.K. Graham, D. DeRyckere, C.C. Porter, and C.J. Henry. 2022. Obesity-induced galectin-9 is a therapeutic target in B-cell acute lymphoblastic leukemia. *Nat Commun*. 13:1157.

Levine, J.H., E.F. Simonds, S.C. Bendall, K.L. Davis, A.D. Amir el, M.D. Tadmor, O. Litvin, H.G. Fienberg, A. Jager, E.R. Zunder, R. Finck, A.L. Gedman, I. Radtke, J.R. Downing, D. Pe'er, and G.P. Nolan. 2015. Data-Driven Phenotypic Dissection of AML Reveals Progenitor-like Cells that Correlate with Prognosis. *Cell*. 162:184-197.

Li, C., Z. Tang, W. Zhang, Z. Ye, and F. Liu. 2021. GEPIA2021: integrating multiple deconvolution-based analysis into GEPIA. *Nucleic Acids Res*. 49:W242-W246.

Lin, J.-R., Y.-A. Chen, D. Campton, J. Cooper, S. Coy, C. Yapp, J.B. Tefft, E. McCarty, K.L. Ligon, S.J. Rodig, S. Reese, T. George, S. Santagata, and P.K. Sorger. 2022. Multi-modal digital pathology for colorectal cancer diagnosis by high-plex immunofluorescence imaging and traditional histology of the same tissue section. *bioRxiv*.

Lin, J.R., B. Izar, S. Wang, C. Yapp, S. Mei, P.M. Shah, S. Santagata, and P.K. Sorger. 2018. Highly multiplexed immunofluorescence imaging of human tissues and tumors using t-CyCIF and conventional optical microscopes. *Elife*. 7.

Liu, B., X. Hu, K. Feng, R. Gao, Z. Xue, S. Zhang, Y. Zhang, E. Corse, Y. Hu, W. Han, and Z. Zhang. 2022. Temporal single-cell tracing reveals clonal revival and expansion of precursor exhausted T cells during anti-PD-1 therapy in lung cancer. *Nat Cancer*. 3:108-121.

McGinnis, C.S., L.M. Murrow, and Z.J. Gartner. 2019. DoubletFinder: Doublet Detection in Single-Cell RNA Sequencing Data Using Artificial Nearest Neighbors. *Cell Syst*. 8:329-337.e324.

McLane, L.M., M.S. Abdel-Hakeem, and E.J. Wherry. 2019. CD8 T Cell Exhaustion During Chronic Viral Infection and Cancer. *Annual review of immunology*. 37:457-495.

Obar, J.J., E.R. Jellison, B.S. Sheridan, D.A. Blair, Q.-M. Pham, J.M. Zickovich, and L. Lefrançois. 2011. Pathogen-Induced Inflammatory Environment Controls Effector and Memory $CD8^+$ T Cell Differentiation. *The Journal of Immunology*. 187:4967-4978.

Oh, D.Y., and L. Fong. 2021. Cytotoxic CD4(+) T cells in cancer: Expanding the immune effector toolbox. *Immunity*. 54:2701-2711.

Oh, D.Y., S.S. Kwek, S.S. Raju, T. Li, E. McCarthy, E. Chow, D. Aran, A. Ilano, C.S. Pai, C. Rancan, K. Allaire, A. Burra, Y. Sun, M.H. Spitzer, S. Mangul, S. Porten, M.V. Meng, T.W. Friedlander, C.J. Ye, and L. Fong. 2020. Intratumoral CD4(+) T Cells Mediate Anti-tumor Cytotoxicity in Human Bladder Cancer. *Cell*. 181:1612-1625.e1613.

Pang, N., X. Alimu, R. Chen, M. Muhashi, J. Ma, G. Chen, F. Zhao, L. Wang, J. Qu, and J. Ding. 2021a. Activated Galectin-9/Tim3 promotes Treg and suppresses Th1 effector function in chronic lymphocytic leukemia. *Faseb j*. 35:e21556.

Pang, N., X. Alimu, R. Chen, M. Muhashi, J. Ma, G. Chen, F. Zhao, L. Wang, J. Qu, and J. Ding. 2021b. Activated Galectin-9/Tim3 promotes Treg and suppresses Th1 effector function in chronic lymphocytic leukemia. *The FASEB Journal*. 35:e21556.

Quezada, S.A., T.R. Simpson, K.S. Peggs, T. Merghoub, J. Vider, X. Fan, R. Blasberg, H. Yagita, P. Muranski, P.A. Antony, N.P. Restifo, and J.P. Allison. 2010. Tumor-reactive CD4(+) T cells develop cytotoxic activity and eradicate large established melanoma after transfer into lymphopenic hosts. *J Exp Med*. 207:637-650.

Reinart, N., P.H. Nguyen, J. Boucas, N. Rosen, H.M. Kvasnicka, L. Heukamp, C. Rudolph, V. Ristovska, T. Velmans, C. Mueller, K.S. Reiners, E.P. von Strandmann, G. Krause, M. Montesinos-Rongen, B. Schlegelberger, M. Herling, M. Hallek, and G. Fingerle-Rowson. 2013. Delayed development of chronic lymphocytic leukemia in the absence of macrophage migration inhibitory factor. *Blood*. 121:812-821.

Roessner, P.M., L. Llaó Cid, E. Lupar, T. Roider, M. Bordas, C. Schifflers, L. Arseni, A.C. Gaupel, F. Kilpert, M. Krötschel, S.J. Arnold, L. Sellner, D. Colomer, S. Stilgenbauer, S. Dietrich, P. Lichter, A. Izcue, and M. Seiffert. 2021. EOMES and IL-10 regulate antitumor activity of T regulatory type 1 CD4(+) T cells in chronic lymphocytic leukemia. *Leukemia*. 35:2311-2324.

Roider, T., M.A. Baertsch, D. Fitzgerald, H. Voehringer, B.J. Brinkmann, F. Czernilofsky, M. Knoll, L. Llao-Cid, P.-M. Bruch, N. Liebers, C.M. Schuerch, V. Passerini, A. Brobeil, G. Mechtersheimer, C. Mueller-Tidow, O. Weigert, M. Seiffert, G.P. Nolan, W. Huber, and S. Dietrich. 2022. Multimodal and spatially resolved profiling identifies distinct patterns of T-cell infiltration in nodal B-cell lymphoma entities. *bioRxiv*:2022.2011.2004.514366.

Sabatos-Peyton, C., T. Longmire, L. Baker, N. Patel, A.-S. Wavreille, M. Verneret, P. Jayaraman, X. Jiang, S. Schwartz, V. Cremasco, H. Lu, S. Qiu, F. Sharp, M. Rinne, and G. Dranoff. 2020. 439 Dual modes of action for anti-TIM-3 antibody MBG453 in myelodysplastic syndromes (MDS) and acute myeloid leukemia (AML): preclinical evidence for immune-mediated and anti-leukemic activity. *Journal for ImmunoTherapy of Cancer*. 8:A267-A267.

Sabatos-Peyton, C.A., J. Nevin, A. Brock, J.D. Venable, D.J. Tan, N. Kassam, F. Xu, J. Taraszka, L. Wesemann, T. Pertel, N. Acharya, M. Klapholz, Y. Etminan, X. Jiang, Y.H. Huang, R.S. Blumberg, V.K. Kuchroo, and A.C. Anderson. 2018. Blockade of Tim-3 binding to phosphatidylserine and CEACAM1 is a shared feature of anti-Tim-3 antibodies that have functional efficacy. *Oncoimmunology*. 7:e1385690.

Saka, S.K., Y. Wang, J.Y. Kishi, A. Zhu, Y. Zeng, W. Xie, K. Kirli, C. Yapp, M. Cicconet, B.J. Beliveau, S.W. Lapan, S. Yin, M. Lin, E.S. Boyden, P.S. Kaeser, G. Pihan, G.M. Church, and P. Yin. 2019. Immuno-SABER enables highly multiplexed and amplified protein imaging in tissues. *Nature biotechnology*. 37:1080-1090.

Sawant, D.V., H. Yano, M. Chikina, Q. Zhang, M. Liao, C. Liu, D.J. Callahan, Z. Sun, T. Sun, T. Tabib, A. Pennathur, D.B. Corry, J.D. Luketich, R. Lafyatis, W. Chen, A.C. Poholek, T.C. Bruno, C.J. Workman, and D.A.A. Vignali. 2019. Adaptive plasticity of IL-10(+) and IL-35(+) T(reg) cells cooperatively promotes tumor T cell exhaustion. *Nat Immunol*. 20:724-735.

Schapiro, D., A. Sokolov, C. Yapp, Y.A. Chen, J.L. Muhlich, J. Hess, A.L. Creason, A.J. Nirmal, G.J. Baker, M.K. Nariya, J.R. Lin, Z. Maliga, C.A. Jacobson, M.W. Hodgman, J. Ruokonen, S.L. Farhi, D. Abbondanza, E.T. McKinley, D. Persson, C. Betts, S. Sivagnanam, A. Regev, J. Goecks, R.J. Coffey, L.M. Coussens, S. Santagata, and P.K. Sorger. 2022. MCMICRO: a scalable, modular image-processing pipeline for multiplexed tissue imaging. *Nat Methods*. 19:311-315.

Scott, A.C., F. Dündar, P. Zumbo, S.S. Chandran, C.A. Klebanoff, M. Shakiba, P. Trivedi, L. Menocal, H. Appleby, S. Camara, D. Zamarin, T. Walther, A. Snyder, M.R. Femia, E.A. Comen, H.Y. Wen, M.D. Hellmann, N. Anandasabapathy, Y. Liu, N.K. Altorki, P. Lauer, O. Levy, M.S. Glickman, J. Kaye, D. Betel, M. Philip, and A. Schietinger. 2019. TOX is a critical regulator of tumour-specific T cell differentiation. *Nature*. 571:270-274.

Şenbabaoğlu, Y., R.S. Gejman, A.G. Winer, M. Liu, E.M. Van Allen, G. de Velasco, D. Miao, I. Ostrovnaya, E. Drill, A. Luna, N. Weinhold, W. Lee, B.J. Manley, D.N. Khalil, S.D. Kaffenberger, Y. Chen, L. Danilova, M.H. Voss, J.A. Coleman, P. Russo, V.E. Reuter, T.A. Chan, E.H. Cheng, D.A. Scheinberg, M.O. Li, T.K. Choueiri, J.J. Hsieh, C. Sander, and A.A. Hakimi. 2016. Tumor immune microenvironment characterization in clear cell renal cell carcinoma identifies prognostic and immunotherapeutically relevant messenger RNA signatures. *Genome Biol*. 17:231.

Tang, Z., B. Kang, C. Li, T. Chen, and Z. Zhang. 2019. GEPIA2: an enhanced web server for large-scale expression profiling and interactive analysis. *Nucleic Acids Res*. 47:W556-w560.

Türei, D., T. Korcsmáros, and J. Saez-Rodriguez. 2016. OmniPath: guidelines and gateway for literature-curated signaling pathway resources. *Nat Methods*. 13:966-967.

Türei, D., A. Valdeolivas, L. Gul, N. Palacio-Escat, M. Klein, O. Ivanova, M. Ölbei, A. Gábor, F. Theis, D. Módos, T. Korcsmáros, and J. Saez-Rodriguez. 2021. Integrated intra- and intercellular signaling knowledge for multicellular omics analysis. *Mol Syst Biol*. 17:e9923.

Utzschneider, D.T., M. Charmoy, V. Chennupati, L. Pousse, D.P. Ferreira, S. Calderon-Copete, M. Danilo, F. Alfei, M. Hofmann, D. Wieland, S. Pradervand, R. Thimme, D. Zehn, and W. Held. 2016. T Cell Factor 1-Expressing Memory-like CD8(+) T Cells Sustain the Immune Response to Chronic Viral Infections. *Immunity*. 45:415-427.

van Bruggen, J.A.C., A.W.J. Martens, J.A. Fraietta, T. Hofland, S.H. Tonino, E. Eldering, M.D. Levin, P.J. Siska, S. Endstra, J.C. Rathmell, C.H. June, D.L. Porter, J.J. Melenhorst, A.P. Kater, and G.J.W. van der Windt. 2019. Chronic lymphocytic leukemia cells impair mitochondrial fitness in CD8(+) T cells and impede CAR T-cell efficacy. *Blood*. 134:44-58.

Van den Berge, K., H. Roux de Bezieux, K. Street, W. Saelens, R. Cannoodt, Y. Saeys, S. Dudoit, and L. Clement. 2020. Trajectory-based differential expression analysis for single-cell sequencing data. *Nat Commun*. 11:1201.

Van Gassen, S., B. Callebaut, M.J. Van Helden, B.N. Lambrecht, P. Demeester, T. Dhaene, and Y. Saeys. 2015. FlowSOM: Using self-organizing maps for visualization and interpretation of cytometry data. *Cytometry A*. 87:636-645.

Vuong, L., R.R. Kotecha, M.H. Voss, and A.A. Hakimi. 2019. Tumor Microenvironment Dynamics in Clear-Cell Renal Cell Carcinoma. *Cancer discovery*. 9:1349-1357.

Wdowiak, K., E. Gallego□Colon, T. Francuz, P. Czajka□Francuz, N. Ruiz□Agamez, M. Kubeczko, I. Grochoła, M.T. Wybraniec, J. Chudek, and J. Wojnar. 2019. Increased serum levels of Galectin□9 in patients with chronic lymphocytic leukemia. *Oncol Lett*. 17:1019-1029.

Wierz, M., S. Pierson, L. Guyonnet, E. Viry, A. Lequeux, A. Oudin, S.P. Niclou, M. Ollert, G. Berchem, B. Janji, C. Guérin, J. Paggetti, and E. Moussay. 2018. Dual PD1/LAG3 immune checkpoint blockade limits tumor development in a murine model of chronic lymphocytic leukemia. *Blood*. 131:1617-1621.

Wilkerson, M.D., and D.N. Hayes. 2010. ConsensusClusterPlus: a class discovery tool with confidence assessments and item tracking. *Bioinformatics*. 26:1572-1573.

Wolf, Y., A.C. Anderson, and V.K. Kuchroo. 2020. TIM3 comes of age as an inhibitory receptor. *Nat Rev Immunol*. 20:173-185.

Xie, Y., A. Akpinarli, C. Maris, E.L. Hipkiss, M. Lane, E.K. Kwon, P. Muranski, N.P. Restifo, and P.A. Antony. 2010. Naive tumor-specific CD4(+) T cells differentiated in vivo eradicate established melanoma. *J Exp Med*. 207:651-667.

Xierenguli, A., X. Zeng, N. Pang, R. Zhagn, J. Ma, Y. Zhao, and J. Qu. 2020. [TIM-3/galectin-9 is involved in negative regulation of T cells in patients with chronic lymphocytic leukemia]. *Xi Bao Yu Fen Zi Mian Yi Xue Za Zhi*. 36:1021-1025.

Xu-Monette, Z.Y., J. Zhou, and K.H. Young. 2018. PD-1 expression and clinical PD-1 blockade in B-cell lymphomas. *Blood*. 131:68-83.

Yan, X.J., E. Albesiano, N. Zanesi, S. Yancopoulos, A. Sawyer, E. Romano, A. Petlickovski, D.G. Efremov, C.M. Croce, and N. Chiorazzi. 2006. B cell receptors in TCL1 transgenic mice resemble those of aggressive, treatment-resistant human chronic lymphocytic leukemia. *Proc Natl Acad Sci U S A*. 103:11713-11718.

Yang, R., L. Sun, C.F. Li, Y.H. Wang, J. Yao, H. Li, M. Yan, W.C. Chang, J.M. Hsu, J.H. Cha, J.L. Hsu, C.W. Chou, X. Sun, Y. Deng, C.K. Chou, D. Yu, and M.C. Hung. 2021. Galectin-9 interacts with PD-1 and TIM-3 to regulate T cell death and is a target for cancer immunotherapy. *Nat Commun*. 12:832.

Yang, R.Y., G.A. Rabinovich, and F.T. Liu. 2008. Galectins: structure, function and therapeutic potential. *Expert Rev Mol Med*. 10:e17.

Yapp, C., E. Novikov, W.D. Jang, T. Vallius, Y.A. Chen, M. Cicconet, Z. Maliga, C.A. Jacobson, D. Wei, S. Santagata, H. Pfister, and P.K. Sorger. 2022. UnMICST: Deep learning with real augmentation for robust segmentation of highly multiplexed images of human tissues. *Commun Biol*. 5:1263.

Yeo, A.T., S. Rawal, B. Delcuze, A. Christofides, A. Atayde, L. Strauss, L. Balaj, V.A. Rogers, E.J. Uhlmann, H. Varma, B.S. Carter, V.A. Boussiotis, and A. Charest. 2022. Single-cell RNA sequencing reveals evolution of immune landscape during glioblastoma progression. *Nat Immunol*. 23:971-984.

Zhang, H., Y.B. Luo, W. Wu, L. Zhang, Z. Wang, Z. Dai, S. Feng, H. Cao, Q. Cheng, and Z. Liu. 2021. The molecular feature of macrophages in tumor immune microenvironment of glioma patients. *Computational and structural biotechnology journal*. 19:4603-4618.

Zheng, L., S. Qin, W. Si, A. Wang, B. Xing, R. Gao, X. Ren, L. Wang, X. Wu, J. Zhang, N. Wu, N. Zhang, H. Zheng, H. Ouyang, K. Chen, Z. Bu, X. Hu, J. Ji, and Z. Zhang. 2021. Pan-cancer single-cell landscape of tumor-infiltrating T cells. *Science*. 374:abe6474.

Zhu, C., A.C. Anderson, A. Schubart, H. Xiong, J. Imitola, S.J. Khoury, X.X. Zheng, T.B. Strom, and V.K. Kuchroo. 2005. The Tim-3 ligand galectin-9 negatively regulates T helper type 1 immunity. *Nat Immunol*. 6:1245-1252.

**Acknowledgements**

We would like to thank all members of the High Throughput Sequencing Unit of the Genomics and Proteomics Core Facility, of the Light Microscopy Core Facility, and of the Single-cell Open Lab (scOpenLab) at the German Cancer Research Center (DKFZ, Heidelberg) for their technical assistance. We also thank the National Cytometry Platform (NCP) of the Luxembourg Institute of Health (LIH, Luxembourg) for assistance with the generation of cytometry data, in particular Maira Konstantinou and Dominique Revets. The NCP is supported by funding from Luxembourg's Ministry of Higher Education and Research (MESR). Tissue microarrays and lymph node sections were provided by the Tissue Bank of the National Center for Tumor Diseases (NCT) Heidelberg, Germany in accordance with the regulations of the tissue bank and the approval of the ethics committee of Heidelberg University.

This study was supported by a research grant of the German Cancer Aid (Deutsche Krebshilfe) to MS, by grants from FNRS-Télévie to IFB (7.4529.19, 7.6603.21), MW (7.6504.18), GP (7.4501.18, 7.6518.20), SG (7.4502.19, 7.6604.21), and from the Luxembourg National Research Fund (FNR), Fondation Cancer and Plooschter Projet to EM and JP (C20/BM/14582635, and C20/BM/14592342). The authors acknowledge support by the state of Baden-Württemberg through bwHPC and the German Research Foundation (DFG) through grant INST 35/1597-1 FUGG. MC, KB and DS are supported by the German Federal Ministry of Education and Research (BMBF 01ZZ2004).

**Author information**

L.L.C. designed the study, performed experiments, analyzed data, generated figures, and wrote the paper. J.K.L.W. performed bioinformatical analyses, generated figures, and wrote the paper. I.F.B. and M.W. conceptualized part of the study, performed experiments, and analyzed data. Y.P. analyzed scRNA-seq data and CyTOF data. A.F. conducted experiments, analyzed data, and generated figures. S.G., G.P., C.S. A.C., F.C., P-M.B. and D.E.C. performed experiments and analyzed data. M.C., K.B. and D.S. analyzed multiplex imaging data, and generated figures. M.I. performed bioinformatical analyses and generated figures. T.R. and S.D. provided input regarding cluster annotations and performed correlation analyses. J.P.M. established the pipeline for single-cell RNA-sequencing. E.G.-H. and A.R. supported the study with lymph node sections and expertise in interpreting imaging data of lymph nodes. D.C., E.C., and S.D. provided clinical samples and information. P.L. provided logistic and budget support and was involved in scientific discussions. E.M., J.P., M.Z., and M.S., conceptualized the study, guided experiments and data analysis, provided logistic and budget support, and wrote the paper.

## Ethics declarations

Samples from patients and heathy controls were obtained after informed consent and according to the guidelines of the Ethics Committees of the involved University hospitals and the Declaration of Helsinki.

All experiments involving laboratory animals were conducted in pathogen-free animal facilities at the German Cancer Research Center in Heidelberg or the Luxembourg Institute of Health in Luxembourg with the approval of the Regierungspräsidium Karlsruhe (G-77/19 and G-112/21) and the Luxembourg Ministry for Agriculture (#LUPA 2019/21), respectively. Mice were treated in accordance with the European guidelines.

## Competing interests

The authors declare no competing interests directly related to this work. The authors however disclose unrelated funding and honorariums as follows: D.S. reports funding from GSK and receives honorariums from immuneai and Alpenglow. M.S. reports research funding from Bayer AG.

## Supplemental Excel Table Titles

**Suppl. Table 1:** Information on patients and donors

**Suppl. Table 2:** Cell cluster annotations

**Suppl. Table 3:** Correlations with clinical data

**Suppl. Table 4:** VDJdb results of TCR-seq data

Figure 1

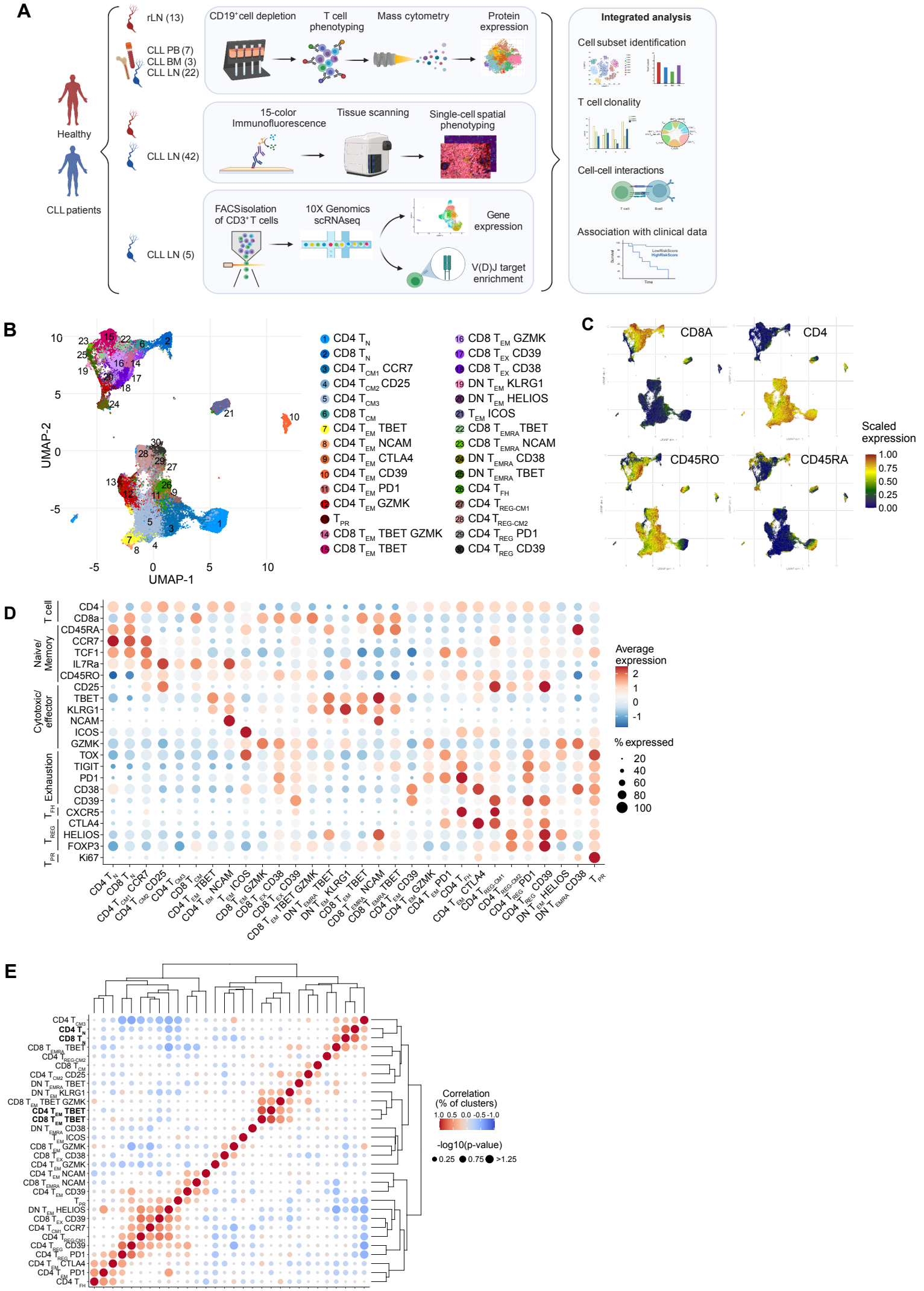
A
Healthy
CLL patients
rLN (13)
CLL PB (7)
CLL BM (3)
CLL LN (22)
CD19+ cell depletion
T cell phenotyping
Mass cytometry
Protein expression
CLL LN (42)
15-color Immunofluorescence
Tissue scanning
Single-cell spatial phenotyping
CLL LN (5)
FACSisolation of CD3+ T cells
10X Genomics scRNAseq
Gene expression
V(D)J target enrichment
Integrated analysis
Cell subset identification
T cell clonality
Cell-cell interactions
Association with clinical data
B
UMAP-1
UMAP-2
1 CD4 TN
2 CD8 TN
3 CD4 TCM1 CCR7
4 CD4 TCM2 CD25
5 CD4 TCM3
6 CD8 TCM
7 CD4 TEM TBET
8 CD4 TEM NCAM
9 CD4 TEM CTLA4
10 CD4 TEM CD39
11 CD4 TEM PD1
12 CD4 TEM GZMK
13 TPR
14 CD8 TEM TBET GZMK
15 CD8 TEM TBET
16 CD8 TEM GZMK
17 CD8 TEX CD39
18 CD8 TEX CD38
19 DN TEM KLRG1
20 DN TEM HELIOS
21 TEM ICOS
22 CD8 TEMRA TBET
23 CD8 TEMRA NCAM
24 DN TEMRA CD38
25 DN TEMRA TBET
26 CD4 TFH
27 CD4 TREG-CM1
28 CD4 TREG-CM2
29 CD4 TREG PD1
30 CD4 TREG CD39
C
CD8A
CD4
CD45RO
CD45RA
Scaled expression
1.00
0.75
0.50
0.25
0.00
D
T cell
Naive/ Memory
Cytotoxic/ effector
Exhaustion
TFH
TREG
TPR
CD4
CD8a
CD45RA
CCR7
TCF1
IL7Ra
CD45RO
CD25
TBET
KLRG1
NCAM
ICOS
GZMK
TOX
TIGIT
PD1
CD38
CD39
CXCR5
CTLA4
HELIOS
FOXP3
Ki67
Average expression
2
1
0
-1
% expressed
20
40
60
80
100
E
Correlation (% of clusters)
1.0 0.5 0.0 -0.5 -1.0
-log10(p-value)
0.25
0.75
>1.25

Figure 2

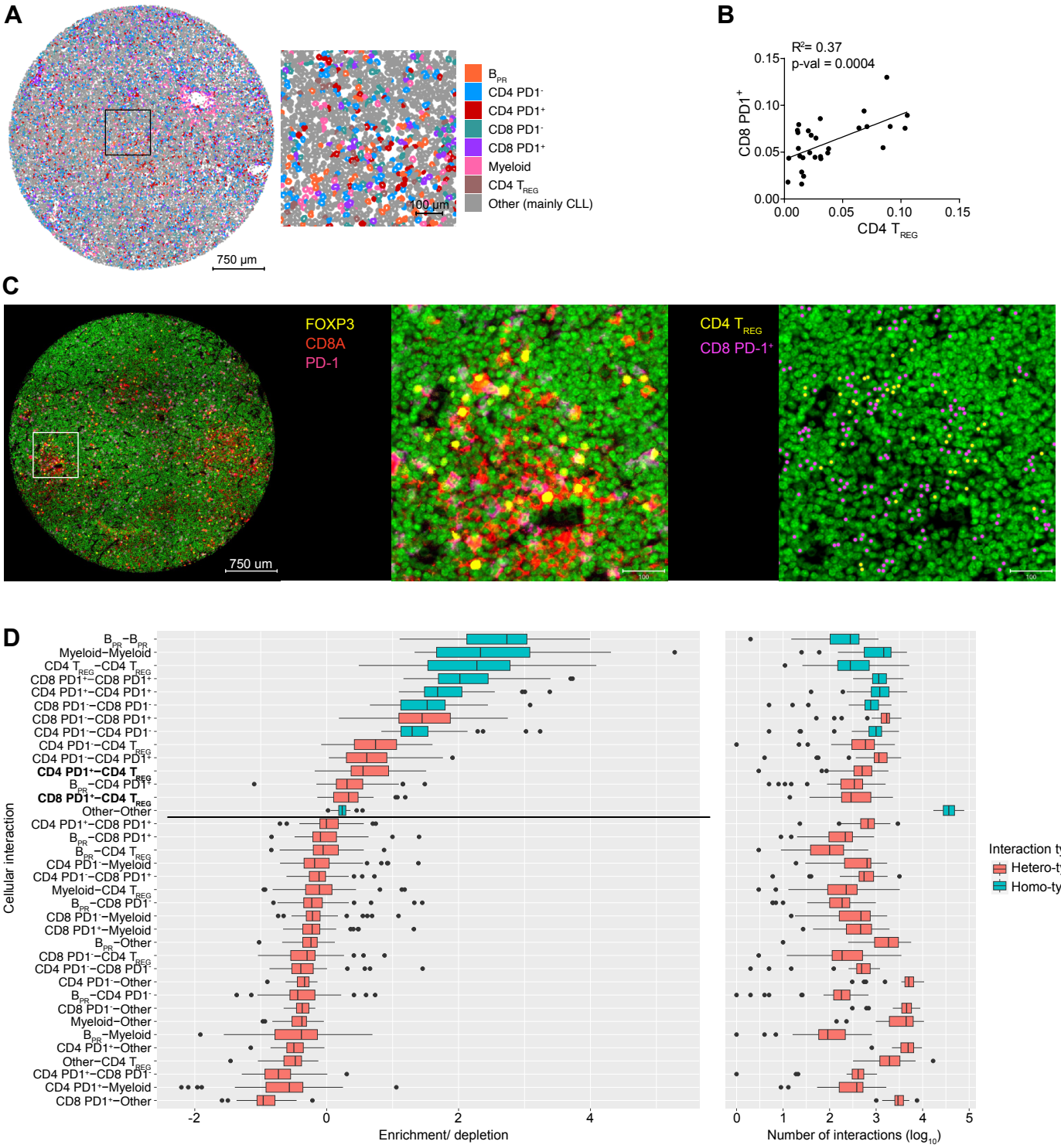
A
750 µm
100 µm
B_PR
CD4 PD1-
CD4 PD1+
CD8 PD1-
CD8 PD1+
Myeloid
CD4 T_REG
Other (mainly CLL)
B
R²= 0.37
p-val = 0.0004
CD8 PD1+
CD4 T_REG
C
FOXP3
CD8A
PD-1
750 um
CD4 T_REG
CD8 PD-1+
D
Cellular interaction
Enrichment/ depletion
Number of interactions (log10)
Interaction type
Hetero-typic
Homo-typic

Figure 3

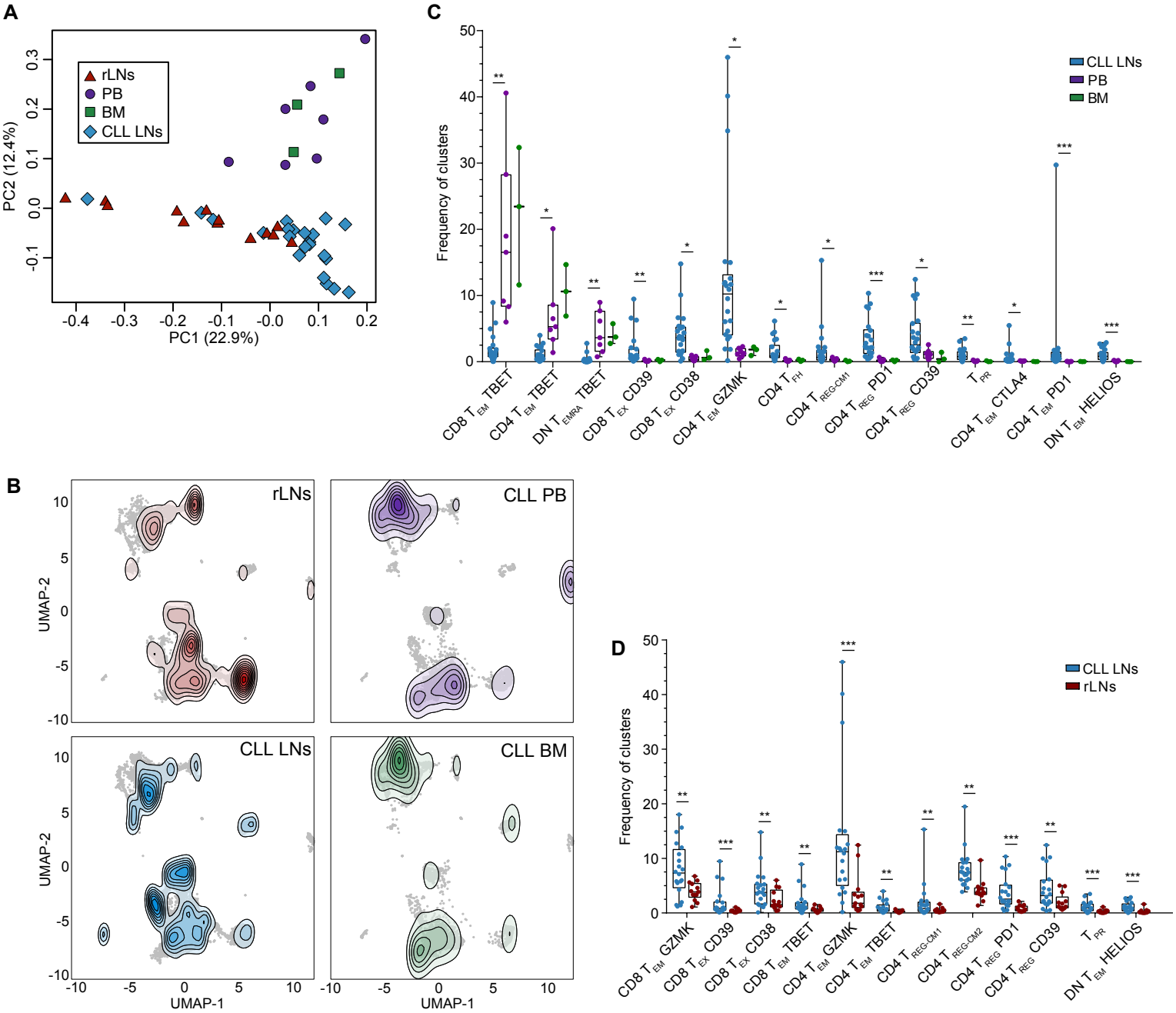
A
rLNs
PB
BM
CLL LNs
PC2 (12.4%)
PC1 (22.9%)
B
rLNs
CLL PB
CLL LNs
CLL BM
UMAP-2
UMAP-1
C
CLL LNs
PB
BM
Frequency of clusters
CD8 T EM TBET
CD4 T EM TBET
DN T EMRA TBET
CD8 T EX CD39
CD8 T EX CD38
CD4 T EM GZMK
CD4 T FH
CD4 T REG-CM1
CD4 T REG PD1
CD4 T REG CD39
T PR
CD4 T EM CTLA4
CD4 T EM PD1
DN T EM HELIOS
D
CLL LNs
rLNs
Frequency of clusters
CD8 T EM GZMK
CD8 T EX CD39
CD8 T EX CD38
CD8 T EM TBET
CD4 T EM GZMK
CD4 T EM TBET
CD4 T REG-CM1
CD4 T REG-CM2
CD4 T REG PD1
CD4 T REG CD39
T PR
DN T EM HELIOS

Figure 4

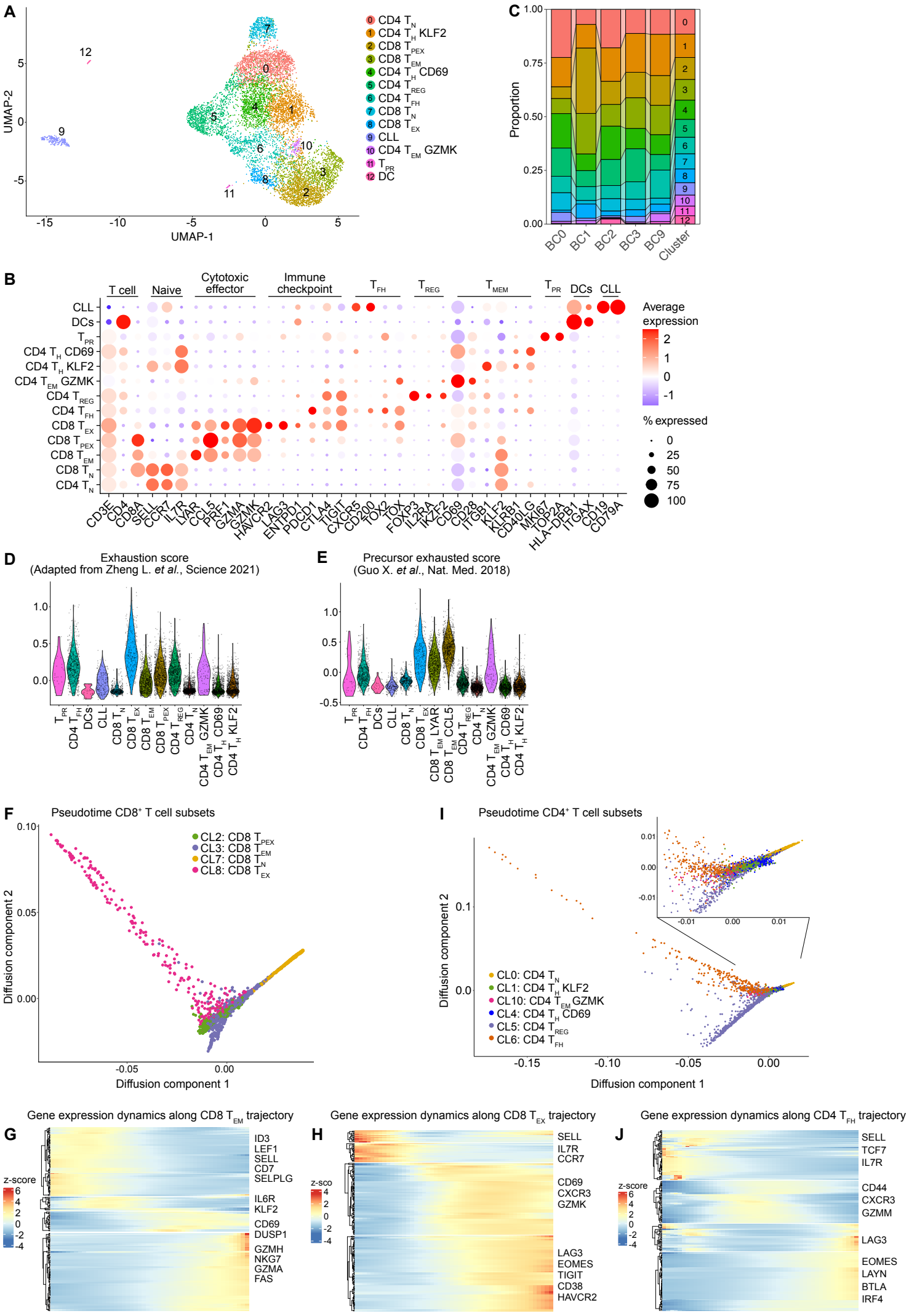
A
UMAP-2
UMAP-1
0 CD4 T_N
1 CD4 T_H KLF2
2 CD8 T_PEX
3 CD8 T_EM
4 CD4 T_H CD69
5 CD4 T_REG
6 CD4 T_FH
7 CD8 T_N
8 CD8 T_EX
9 CLL
10 CD4 T_EM GZMK
11 T_PR
12 DC
C
Proportion
BC0
BC1
BC2
BC3
BC9
Cluster
B
T cell
Naive
Cytotoxic effector
Immune checkpoint
T_FH
T_REG
T_MEM
T_PR
DCs
CLL
Average expression
% expressed
CD3E CD4 CD8A SELL CCR7 IL7R LYAR CCL5 PRF1 GZMA GZMK HAVCR2 LAG3 ENTPD1 PDCD1 CTLA4 TIGIT CXCR5 CD200 TOX2 TOX FOXP3 IL2RA IKZF2 CD69 CD28 ITGB1 KLF2 KLRB1 CD40LG MKI67 TOP2A HLA-DPB1 ITGAX CD19 CD79A
D
Exhaustion score
(Adapted from Zheng L. et al., Science 2021)
E
Precursor exhausted score
(Guo X. et al., Nat. Med. 2018)
F
Pseudotime CD8+ T cell subsets
CL2: CD8 T_PEX
CL3: CD8 T_EM
CL7: CD8 T_N
CL8: CD8 T_EX
Diffusion component 2
Diffusion component 1
I
Pseudotime CD4+ T cell subsets
CL0: CD4 T_N
CL1: CD4 T_H KLF2
CL10: CD4 T_EM GZMK
CL4: CD4 T_H CD69
CL5: CD4 T_REG
CL6: CD4 T_FH
Diffusion component 2
Diffusion component 1
Gene expression dynamics along CD8 T_EM trajectory
G
z-score
ID3
LEF1
SELL
CD7
SELPLG
IL6R
KLF2
CD69
DUSP1
GZMH
NKG7
GZMA
FAS
Gene expression dynamics along CD8 T_EX trajectory
H
SELL
IL7R
CCR7
CD69
CXCR3
GZMK
LAG3
EOMES
TIGIT
CD38
HAVCR2
Gene expression dynamics along CD4 T_FH trajectory
J
SELL
TCF7
IL7R
CD44
CXCR3
GZMM
LAG3
EOMES
LAYN
BTLA
IRF4

Figure 5

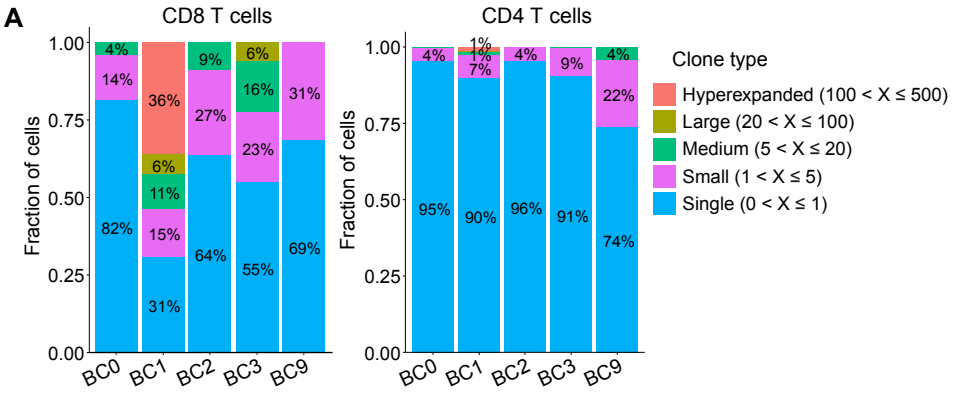
A
CD8 T cells
CD4 T cells
Fraction of cells
1.00
0.75
0.50
0.25
0.00
BC0
BC1
BC2
BC3
BC9
4%
14%
82%
36%
6%
11%
15%
31%
9%
27%
64%
6%
16%
23%
55%
31%
69%
1%
1%
7%
4%
95%
90%
4%
96%
9%
91%
4%
22%
74%
Clone type
Hyperexpanded (100 < X ≤ 500)
Large (20 < X ≤ 100)
Medium (5 < X ≤ 20)
Small (1 < X ≤ 5)
Single (0 < X ≤ 1)

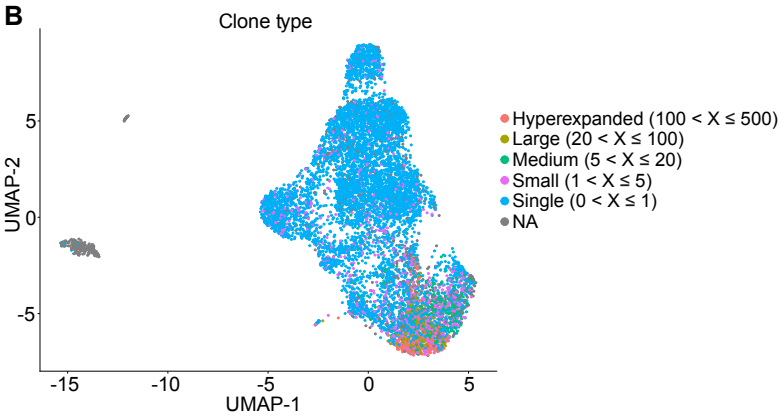
B
Clone type
UMAP-2
UMAP-1
5
0
-5
-15
-10
-5
0
5
Hyperexpanded (100 < X ≤ 500)
Large (20 < X ≤ 100)
Medium (5 < X ≤ 20)
Small (1 < X ≤ 5)
Single (0 < X ≤ 1)
NA

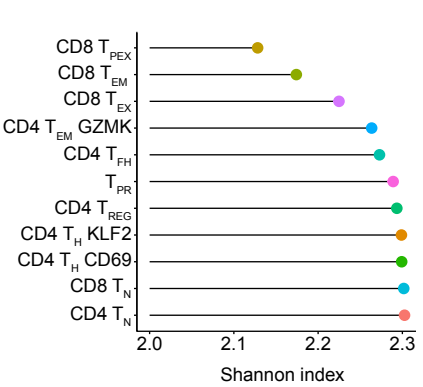
C
CD8 T PEX
CD8 T EM
CD8 T EX
CD4 T EM GZMK
CD4 T FH
T PR
CD4 T REG
CD4 T H KLF2
CD4 T H CD69
CD8 T N
CD4 T N
2.0
2.1
2.2
2.3
Shannon index

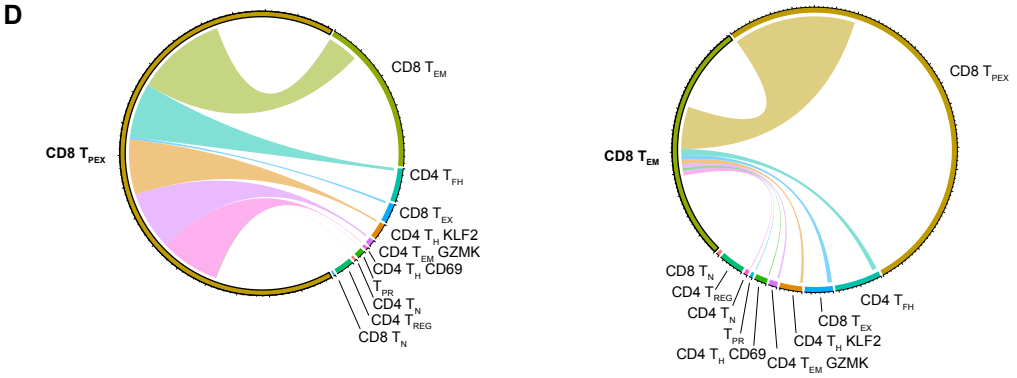
D
CD8 T PEX
CD8 T EM
CD4 T FH
CD8 T EX
CD4 T H KLF2
CD4 T EM GZMK
CD4 T H CD69
T PR
CD4 T N
CD4 T REG
CD8 T N
CD8 T EM
CD8 T PEX
CD8 T N
CD4 T REG
CD4 T N
T PR
CD4 T H CD69
CD4 T EM GZMK
CD4 T H KLF2
CD8 T EX
CD4 T FH

Figure 6

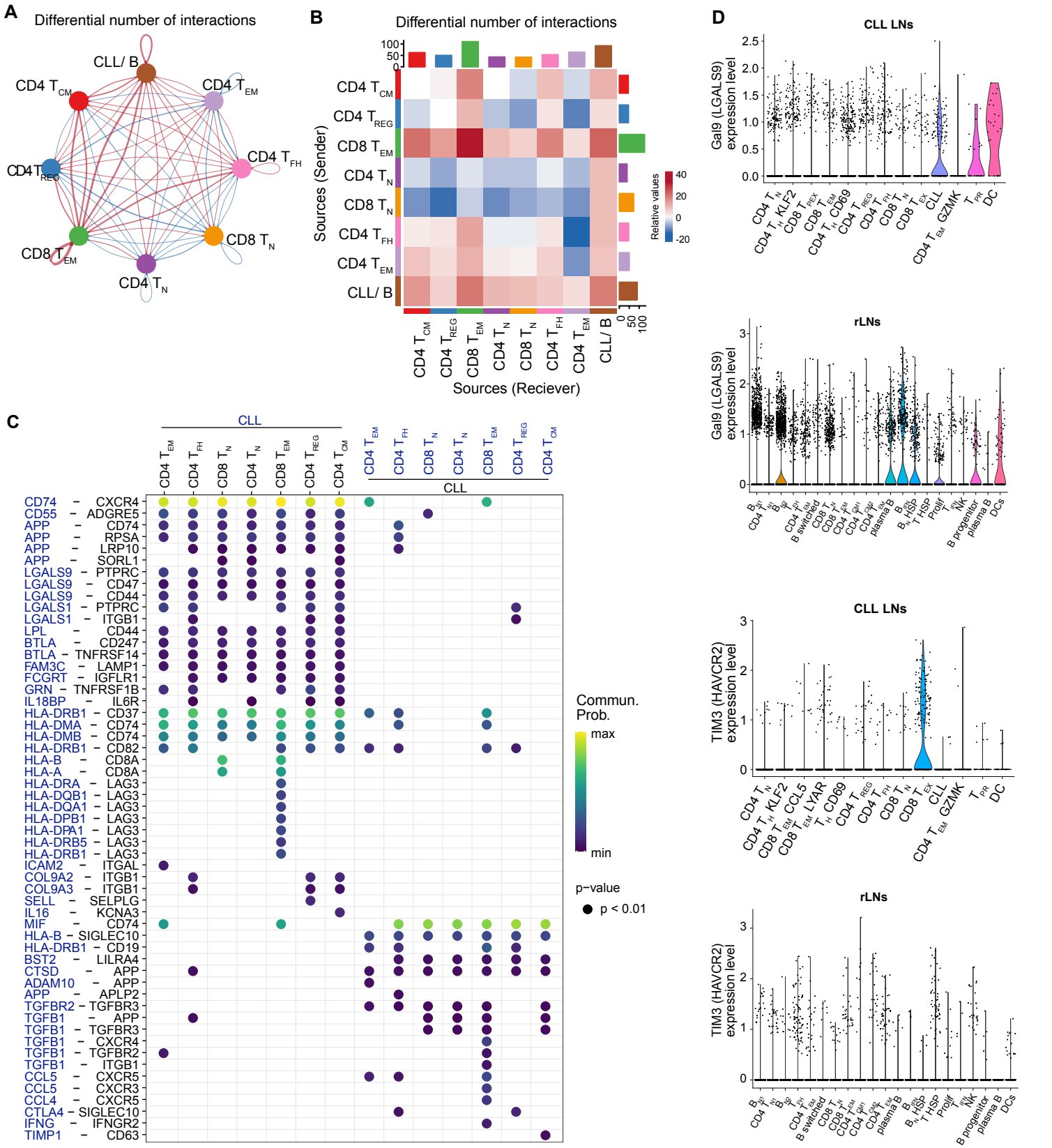
A
Differential number of interactions
CLL/ B
CD4 T CM
CD4 T EM
CD4 T FH
CD4 T REG
CD8 T N
CD8 T EM
CD4 T N
B
Differential number of interactions
Sources (Sender)
Sources (Reciever)
Relative values
C
CLL
CD74 - CXCR4
CD55 - ADGRE5
APP - CD74
APP - RPSA
APP - LRP10
APP - SORL1
LGALS9 - PTPRC
LGALS9 - CD47
LGALS9 - CD44
LGALS1 - PTPRC
LGALS1 - ITGB1
LPL - CD44
BTLA - CD247
BTLA - TNFRSF14
FAM3C - LAMP1
FCGRT - IGFLR1
GRN - TNFRSF1B
IL18BP - IL6R
HLA-DRB1 - CD37
HLA-DMA - CD74
HLA-DMB - CD74
HLA-DRB1 - CD82
HLA-B - CD8A
HLA-A - CD8A
HLA-DRA - LAG3
HLA-DQB1 - LAG3
HLA-DQA1 - LAG3
HLA-DPB1 - LAG3
HLA-DPA1 - LAG3
HLA-DRB5 - LAG3
HLA-DRB1 - LAG3
ICAM2 - ITGAL
COL9A2 - ITGB1
COL9A3 - ITGB1
SELL - SELPLG
IL16 - KCNA3
MIF - CD74
HLA-B - SIGLEC10
HLA-DRB1 - CD19
BST2 - LILRA4
CTSD - APP
ADAM10 - APP
APP - APLP2
TGFBR2 - TGFBR3
TGFB1 - APP
TGFB1 - TGFBR3
TGFB1 - CXCR4
TGFB1 - TGFBR2
TGFB1 - ITGB1
CCL5 - CXCR5
CCL5 - CXCR3
CCL4 - CXCR5
CTLA4 - SIGLEC10
IFNG - IFNGR2
TIMP1 - CD63
Commun. Prob.
max
min
p-value
p < 0.01
D
CLL LNs
rLNs
Gal9 (LGALS9) expression level
TIM3 (HAVCR2) expression level
E
CD3
CD8
DAPI
TIM3
50 µm

Figure 7

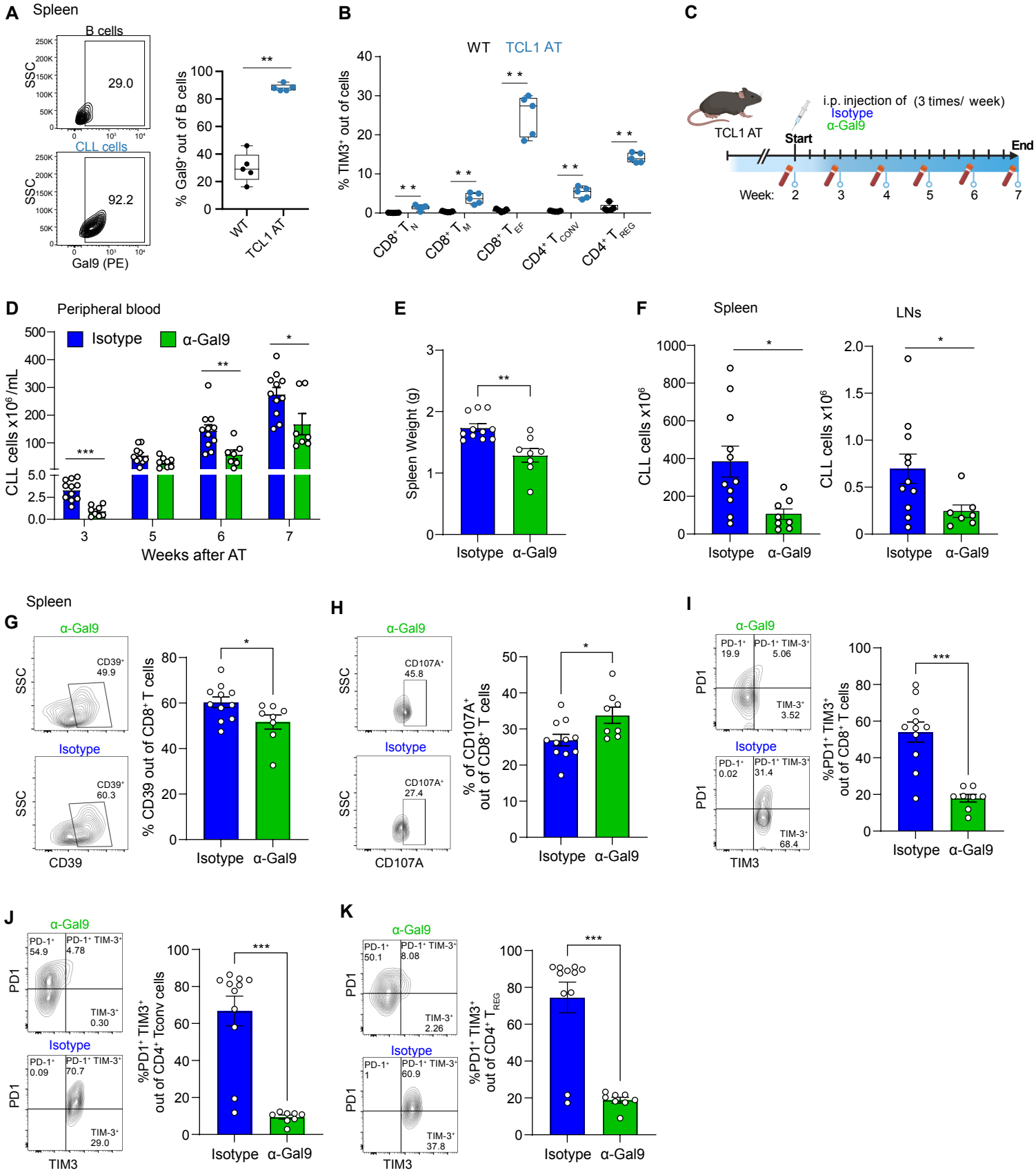
A
Spleen
B cells
29.0
CLL cells
92.2
SSC
Gal9 (PE)
% Gal9+ out of B cells
WT
TCL1 AT
B
WT
TCL1 AT
% TIM3+ out of cells
CD8+ TN
CD8+ TM
CD8+ TEF
CD4+ TCONV
CD4+ TREG
C
TCL1 AT
i.p. injection of (3 times/ week)
Isotype
α-Gal9
Start
End
Week: 2 3 4 5 6 7
D
Peripheral blood
Isotype
α-Gal9
CLL cells x10^6 /mL
Weeks after AT
E
Spleen Weight (g)
Isotype
α-Gal9
F
Spleen
LNs
CLL cells x10^6
Isotype
α-Gal9
G
Spleen
α-Gal9
CD39+ 49.9
Isotype
CD39+ 60.3
SSC
CD39
% CD39 out of CD8+ T cells
Isotype
α-Gal9
H
α-Gal9
CD107A+ 45.8
Isotype
CD107A+ 27.4
SSC
CD107A
% of CD107A+ out of CD8+ T cells
Isotype
α-Gal9
I
α-Gal9
PD-1+ 19.9
PD-1+ TIM-3+ 5.06
TIM-3+ 3.52
Isotype
PD-1+ 0.02
PD-1+ TIM-3+ 31.4
TIM-3+ 68.4
PD1
TIM3
%PD1+ TIM3+ out of CD8+ T cells
Isotype
α-Gal9
J
α-Gal9
PD-1+ 54.9
PD-1+ TIM-3+ 4.78
TIM-3+ 0.30
Isotype
PD-1+ 0.09
PD-1+ TIM-3+ 70.7
TIM-3+ 29.0
PD1
TIM3
%PD1+ TIM3+ out of CD4+ Tconv cells
Isotype
α-Gal9
K
α-Gal9
PD-1+ 50.1
PD-1+ TIM-3+ 8.08
TIM-3+ 2.26
Isotype
PD-1+ 1
PD-1+ TIM-3+ 60.9
TIM-3+ 37.8
PD1
TIM3
%PD1+ TIM3+ out of CD4+ TREG
Isotype
α-Gal9

Figure 8

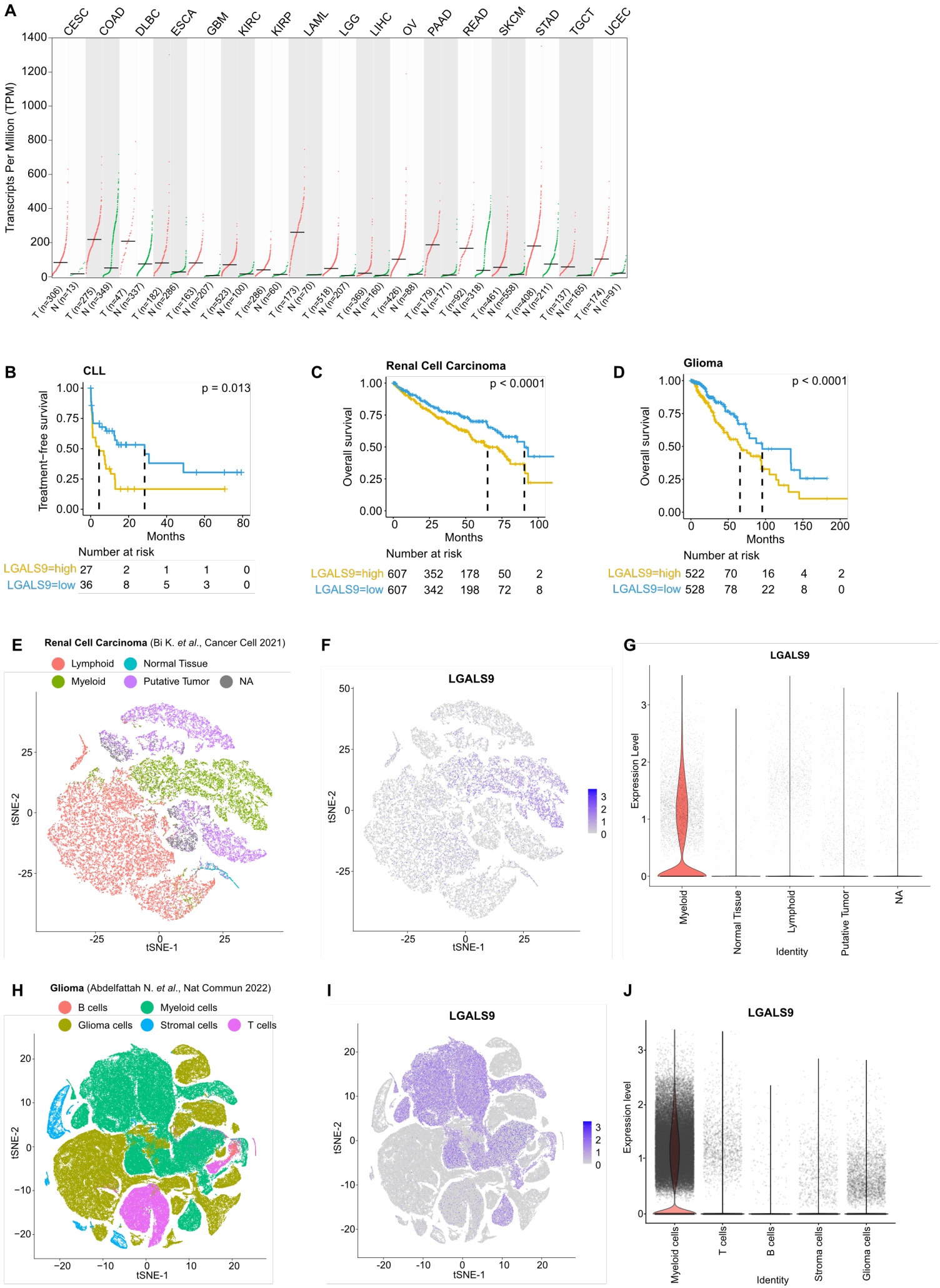
A
CESC
COAD
DLBC
ESCA
GBM
KIRC
KIRP
LAML
LGG
LIHC
OV
PAAD
READ
SKCM
STAD
TGCT
UCEC
Transcripts Per Million (TPM)
B
CLL
p = 0.013
Treatment-free survival
Months
Number at risk
LGALS9=high 27 2 1 1 0
LGALS9=low 36 8 5 3 0
C
Renal Cell Carcinoma
p < 0.0001
Overall survival
Months
Number at risk
LGALS9=high 607 352 178 50 2
LGALS9=low 607 342 198 72 8
D
Glioma
p < 0.0001
Overall survival
Months
Number at risk
LGALS9=high 522 70 16 4 2
LGALS9=low 528 78 22 8 0
E
Renal Cell Carcinoma (Bi K. et al., Cancer Cell 2021)
Lymphoid
Normal Tissue
Myeloid
Putative Tumor
NA
tSNE-1
tSNE-2
F
LGALS9
tSNE-1
tSNE-2
G
LGALS9
Expression Level
Myeloid
Normal Tissue
Lymphoid
Putative Tumor
NA
Identity
H
Glioma (Abdelfattah N. et al., Nat Commun 2022)
B cells
Myeloid cells
Glioma cells
Stromal cells
T cells
tSNE-1
tSNE-2
I
LGALS9
tSNE-1
tSNE-2
J
LGALS9
Expression level
Myeloid cells
T cells
B cells
Stroma cells
Glioma cells
Identity